Three-dimensionality of Vertical Axis Cross-Flow Turbine Flow In High Confinement

Binyu Long

A thesis
submitted in partial fulfillment of the
requirements for the degree of

MASTER OF SCIENCE IN AERONAUTICS & ASTRONAUTICS

University of Washington

2024

Committee:

Owen J. H. Williams

Robert Breidenthal

Program Authorized to Offer Degree:
College of Engineering

University of Washington

Abstract

Three-dimensionality of Vertical Axis Cross-Flow Turbine Flow In High Confinement

Binyu Long

Chair of the Supervisory Committee:
Owen J. H. Williams
Aeronautics & Astronautics

This study explores the three-dimensional hydrodynamics of the wake of cross-flow turbines at high confinement levels—35%, 45%, and 55% of the flow area. Under these conditions, significant increases in power output have been observed, however, the evolution of the flow field and the extent of three-dimensionality has remained to be explored. This work aims to advance the understanding by reconstructing phase-dependent, volumetric three-dimensional flow fields in the near-wake of a pair of counter-rotating cross-flow turbines under different blockages at optimum tip speed ratios. Stereo Particle Image Velocimetry (PIV) data was recorded at three cross-stream stations behind the turbines (x/D = 0.6,1.0,1.5) allowing for an exploration of the flow evolution in the turbine wake. The flow field at each station is correlated to determine a characteristic convective velocity of the dominant vortical structures. Using this result, the planar three-dimensional fields are converted and blended into a comprehensive volumetric flow field for each condition. Various assumptions of the methodology used to construct the volumetric field are investigated. The reconstructed flow field reveals that the wake flow behind the turbine is asymmetrical and three-dimensional, with a marked dependency on the blockage ratio and the phase angle of the turbine. At higher blockage levels, both the vortex structure strength and the velocity of the flow bypassing the turbine increase significantly, thereby facilitating faster wake recovery directly behind the turbine. The streamwise vortices are categorized into four types: blade tip vortices, cross-

pattern vortices, and shear layer vortices directly above and below the wake. Each type of vortex distinctly impacts the flow and fluid momentum distribution behind the turbines. These vortices, convected by local flow velocity gradients, interact with each other and are also attenuated by dissipation. While the vortex structure profiles remain similar under different blockages at their respective optimum tip speed ratios, the strength and distribution of each vortex type are affected differently when conditions change, leading to slight shifts in their relative locations. These variations in vortex structure significantly influence the convective flow field, amplifying the change of vortex evolution as they move downstream. This, in turn, results in marked changes in the shape of the wake flow and bypass flow region. These observations underscore the complex interactions and evolution of fluid structures as they are convected downstream.

TABLE OF CONTENTS

LIST OF FIGURES

LIST OF TABLES

NOMENCLATURE

A: Area

β: Blockage ratio

C: Chord Length

C_p: Coefficient of Power

c: Convective Speed

D: Turbine Diameter

d: Column Vector Rank Difference

Fr: Froude Number

g: Gravitational Acceleration

H: Blade Span

HS: Half Span of Blades

h: Dynamic Flume Water Depth

∞: Free Stream Condition

λ: Tip Speed Ratio

μ: Mean Value

n: Vector Length

ν: Kinematic Viscosity

Ω: Turbine Radial Velocity

ω: Vorticity

R: Turbine Radius

Re: Reynolds Number

r_s: Spearman's Rho Correlation Coefficient

σ: Standard Deviation

T: Temperature

t: Time

θ: Turbine Phase Angle

U: Velocity

W: Weight Function

w: Channel Width

x: Streamwise Coordinates

y: Lateral Coordinates

z: Vertical Coordinates

$|...|$: Vector Magnitude

ACKNOWLEDGMENTS

I wish to express my gratitude to my faculty advisor, Owen Williams, for his patience, immense knowledge, and support for me. His invaluable guidance helped me tremendously throughout every stage of this project and my academic growth.

Furthermore, I extend my heartfelt appreciation to my research group peer, Ari, for dedicating much time and effort to help me with the data acquisition and analysis. His work cleared many obstacles for this project and played a pivotal role in bringing this thesis to fruition.

Lastly, I want to thank committee member, Robert Breidenthal, for assisting me in refining this thesis with their insightful comments and suggestions. His contribution has greatly enhanced the quality and rigor of this work.

DEDICATION

This thesis work is dedicated to my parents, who have provided unconditional love and invaluable guidance throughout my life, encouraging me to pursue my passion for becoming an aeronautical engineer. It is also dedicated to my wife, Vicky. I am truly grateful for your support and for marrying me during the challenging years of graduate school. The difficult days become much brighter when you are with me.

Chapter 1

INTRODUCTION

Renewable energy has become increasingly popular in the 21st century due to concerns over pollution and the rising costs of fossil fuels. Turbines that harness energy from water flow or wind are emerging as a promising clean energy solution for many communities. However, their energy density remains significantly lower than that of fossil fuels. Traditional axial-mounted turbines require high-velocity, undisturbed air, and large radial blades to operate efficiently [3]. These stringent requirements reduce the density of wind farms and necessitate advanced manufacturing techniques to construct slender blades with high structural integrity, increasing operating and maintenance costs. Cross-flow turbines (CFT) circumvent these challenges by mounting blades parallel to the axis of rotation at an offset distance, allowing for increasing the swept area by changing blade length without expanding the turbine's footprint. This design provides a more rigid structure with a smaller footprint than their axial counterparts and makes the turbines less sensitive to the direction of incoming flow, reducing site selection constraints. Moreover, studies have shown that CFT arrays can achieve constructive interference, enhancing overall energy efficiency when installed properly close together [4]. CFTs are also found to have shorter wake recovery distances downstream compared to typical axial turbines [5], facilitating a denser array layout that is both feasible and advantageous, markedly improving the energy density of the wind farm. Additionally, it has been shown that the confinement effect caused by the turbine blocking the flow can increase the amount of flow that is forced through the turbine, thereby further improving the power production of CFT arrays [6]. Consequently, this work focuses on studying the flow around cases with a counter-rotating turbine array with zero blade phase angle offset, which has shown a more constructive influence compared to other rotation schemes in past

studies [5], in high confinement settings to gain insights into improving CFT designs that maximize its unique characteristics and advantages.

Despite the theoretical advantages of cross-flow turbines, their large-scale implementation has not yet been fully realized due to complex hydrodynamics within the flow. This complexity makes optimizing performance under the constantly varying operational conditions in the real world a challenging task. The turbine blades undergo significant changes in angle of attack (AOA), leading to dynamic stall and periodic vortex shedding [7]. These phenomena significantly affect the hydrodynamics and turbine power generation and efficiency. The onset of the dynamic stall is demonstrated to be related to the turbine rotation rate[8], characterized by the tip speed ratio (λ) and is defined as

$$\lambda = \frac{R\Omega}{U\infty} \tag{1.1}$$

where R is the turbine radius to the quarter chord and the Ω is the rotational velocity of the turbine. It has been shown that the size, strength, and convection speed of the shed vortices are highly dependent on λ [9].

High-fidelity three-dimensional CFD simulations of CFTs, especially for large arrays, remain prohibitively expensive today. To simplify the flow calculations around CFTs, several past studies have proposed reducing the simulations to 2D [10] or employing planar particle image velocimetry (PIV) [7] [9]. Howell et al. (2010) [11] assessed the fidelity of 2D and 3D simulations of a CFT in comparison with experimental data, finding that the 2D simulations did not match the experimentally measured turbine performance values as accurately as the 3D simulations. This discrepancy was attributed to the absence of tip vortices in the 2D simulations, which are present in the 3D simulations and experiments. However, this study still lacks the experimentally measured velocity fields needed to validate their 3D simulation results, likely due to difficulties in measuring the flow field near the blades. Other simplified models, such as the blade element momentum, actuator line model, and actuator swept surface model, typically use the lift and drag tables based on the nominal angle of attack, derived from the unperturbed bulk velocity due to the turbine's rotation. This approach

often differs significantly from the actual AOA calculated from the instantaneous flow field [2], due to the presence of flow induction. Furthermore, the onset of dynamic stall further deviates the blade forces from those predicted under empirical steady-state flow conditions [9].

Ryan et al. (2015) [2] used magnetic resonance velocimetry (MRV) to capture the three-dimensional mean velocity field of a CFT, offering insights into the trajectory of tip vortices, top and bottom shear layers, and the asymmetrical wake recovery of the CFT. However, due to limitations in MRV test section size and temporal resolution, the Reynolds number was much lower than in practical applications. More importantly, the instantaneous development of each structure could not be captured in the presented mean field. The 2D planar PIV experiments by Snortland et al. (2020) [8] revealed intriguing hydrodynamics and flow patterns by analyzing horizontal PIV data at the mid-span of a CFT where it was assumed that vertical fluid motion is minimized. They found a strong correlation between near-blade hydrodynamics and the blade's azimuth position, highlighting the importance of investigating instantaneous phase-angle-dependent flow fields to understand the evolution of fluid structures better. Consequently, a robust understanding of the three-dimensional, asymmetrical features and the fluid-structure interactions around the turbine is crucial for developing effective control strategies, CFT array design, and efficiency improvement.

When optimizing the configuration of a cross-flow turbine (CFT) array, flow confinement has been shown to enhance the turbine's power output [12]. This effect of confinement can be quantified using the blockage ratio β, defined by the equation:

$$\beta = \frac{A_{Turbine}}{A_{Channel}} \tag{1.2}$$

where $A_{Turbine}$ represents the turbine's projected area, and $A_{Channel}$ is the total cross-sectional area of the channel. As β increases, the turbine presents greater resistance to the incoming flow. This resistance, combined with the effects of confinement, causes the flow to accelerate as it passes through the turbine, thereby enhancing its performance compared to the same turbine in an unconfined flow. In past studies, this change in performance due to

confinement has been accounted for based on linear momentum theory and the bluff body theory of Maskell[13]. Additionally, a higher blockage ratio is demonstrated to accelerate the flow passing through and around the turbine, as well as narrow the turbine wake[6], which may produce a more pronounced three-dimensional structure and more complex interaction between them, providing higher significance and border implication for studying the three-dimensional cases with high confinement investigated in this work.

This work aims to reconstruct a high-resolution (in space and time) three-dimensional volumetric flow field in the near wake region of an array comprising a pair of counter-rotating cross-flow turbines (CFTs) under three different blockage and tip speed ratios so that we can better study the influences of three-dimensionality and wake evolution at high confinement. Given the demonstrated importance of understanding how blockage influences a turbine's wake at peak power for optimizing array designs [6], this study will exclusively analyze the cases with λ that yield the best performance in each β. Stereo particle image velocimetry (PIV) is used to capture the 3D flow at transverse planes located 0.6, 1.0, and 1.0 diameters downstream from the CFT array center, at 35%, 45%, and 55% blockage and optimal tip speed ratios (TSR) as determined by Hunt (2024) [13]. Since the tip speed ratio (λ) is adjusted alongside the blockage ratio (β), isolating the impact of each variable can be challenging. However, hypotheses can still be formulated regarding their individual effects. The flow fields at each station are correlated with subsequent downstream locations to identify characteristic convective velocities using the frozen flow hypothesis. These results allow fields at each position to be extruded and blended using a weighting function, creating a coherent volumetric flow across the domain of interest. The fluid structures around the turbines are then analyzed by mapping iso-surfaces (velocity, vorticity, etc.) derived from the volumetric flow field. This analysis helps quantify the three-dimensionality of the mean and instantaneous fields, exploring their relationships to blockage, TSR, and their downstream position. Additionally, the vortex structures identified in the volumetric flow field will be discussed for their potential impacts on turbine wake evolution and recovery.

Chapter 2

EXPERIMENTAL APPARATUS & METHODS

2.1 Cross-Flow Turbine Test Setup

Experiments were conducted in the Alice C. Tyler flume at the University of Washington's Harris Hydrodynamics lab. The flume has a test section with a width (w) of 0.76 m and a length of 4.88 m that can accommodate water with depth up to 0.6 m and recirculating flow speed close to $1.1m/s$. Water temperature of $10 - 40°$ can be maintained within the flume with equipped heater and chiller. The capability of the flume ensures that blockage β, free stream velocity U_∞, and temperature requirements in each testing condition investigated can be satisfied.

The tested CFT model, shown in Fig 2.1 comprises a pair of mirrored, counter-rotating identical CFTs installed across the flume. Each turbine features two straight blades, positioned 180° apart, and equipped with symmetrical NACA 0018 profiles with a chord length of 0.0742 m. These blades are affixed to the rotor via hydrodynamic blade-end struts with NACA 0008 profiles, also with a chord length of $C = 0.0742$ m. Additionally, the blades are set at a preset toe-out pitch angle of $-6°$ at a radius of $R = 0.151$ m, measured from the quarter chord. Consequently, the resulting blade quarter chord distance is $D = 0.314$ m, and due to foil thickness, the swept diameter becomes $D' = 0.315$ m. The cord-to-radius ratio is 0.49. The span of the turbine blade is 0.215 m.

Fig. 2.2 illustrates the top view of the tested turbine array. The lateral distance between each turbine center shaft is 1.2D, and the blade-to-blade distance between the turbines (0.22D, 0.93c) is double that of the blade-to-wall distance, ensuring that the wall corresponds to the symmetrical plane of a larger array. The turbines operate in a counter-rotating

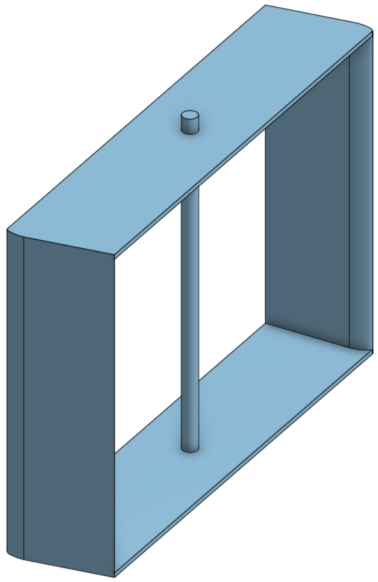

Figure 2.1: Computer Aided Design (CAD) Model of a single tested CFT

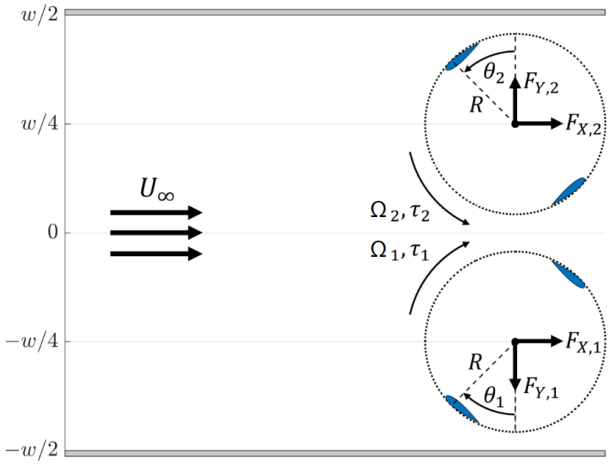

Figure 2.2: Top view of the CFT array layout as installed in the flume[1]. The dashed blue line corresponds to the outermost swept diameter. The rotation angle and direction of each turbine are as indicated by θ and Ω

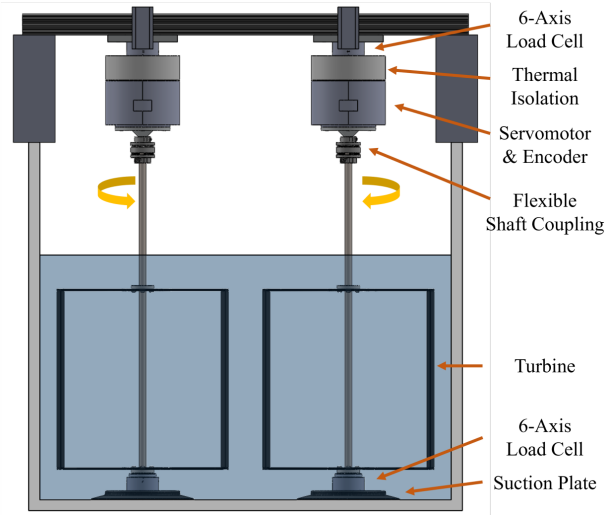

Figure 2.3: View of the CFT test rig in the downstream direction[1]. The rendering is true to scale, and the testing equipment is as listed.

constant speed manner, with a maintained zero phase angle offset. This rotational scheme has been demonstrated to yield the highest performance increase compared to others [14]. The zero phase angle offset ensures that the hydrodynamics are symmetrical across the flume's lateral center plane, allowing analysis to focus solely on the region behind one turbine (Turbine B in the figure). The maintenance of the zero phase angle offset is achieved through a closed-loop controller, with an error tolerance of $\pm 1^\circ$ during the experiment.

The schematic in Fig. 2.3 illustrates how the two rotors are connected to the remainder of the testing apparatus. Positioned atop each turbine shaft is a flexible coupling (Zero-Max SC040R), linking it to a servomotor (Yaskawa SGMCS-05BC341) responsible for modulating the rotation rate of the turbine. The servomotor encoder monitors the θ of each blade, from which the rotation rate is derived.

Furthermore, each turbine is equipped with a pair of 6-axis load cells to measure the net forces and torques. This setup includes an upper load cell (ATI Mini45-IP65) attached to the servomotor and secured to a crossbeam, as well as a lower load cell (ATI Mini45-IP68)

β [%]	λ	h [m]	U_∞ [m/s]	T [°C]	Fr_h	Re_D
36.7	2.6	0.485	0.477	25.4		
45.0	2.9	0.396	0.431	30.1	0.22	1.62×10^5
55.0	3.6	0.324	0.390	35.0		

Table 2.1: Nominal parameters for different blockage conditions.

fixed to the bottom bearing and attached to the flume's bottom via a suction plate to reduce turbine vibration. Data from the load cells, along with information from the servomotor encoders, is collected simultaneously using four National Instruments PCIe-6353 DAQs and synchronized through MATLAB at a frequency of 1000 Hz.

An acoustic Doppler velocimeter (Nortek Vectrino Profiler), situated far upstream of the turbine, measures the freestream velocity at a sample rate of 16 Hz. Positioned at the flume's lateral mid-plane and vertical center of the turbine array, it provides crucial velocity data. Additionally, an ultrasonic free-surface transducer (Omega LVU 32), sampling at 0.5 Hz forward of the turbine array center line, monitors the water depth.

Moreover, the fluid temperature is closely monitored with a temperature probe (Omega Ultra-Precise RTD) and rigorously maintained within $\pm 0.1°C$ of the specified value under each testing condition. These meticulous controls ensure the accuracy and consistency of experimental results.

2.2 Testing Conditions

The blockage ratio of the investigated turbine array is defined as:

$$\beta = \frac{A_{\text{Turbine}}}{A_{\text{Channel}}} = \frac{2HD'}{hw} \tag{2.1}$$

Here, H represents the blade span, h denotes the dynamic water depth, and w indicates the channel width. The blockage ratio can be adjusted by varying the depth of the flume

water while keeping the array geometry constant. Alternative methods for modifying β have been explored in this study [1], and their influence on turbine performance is found to be negligible. To ensure that the blockage effect on the turbine array performance is isolated, it is crucial to control the following non-dimensional flow parameters accordingly.

For this experiment, the Froude number can be defined as:

$$Fr_h = \frac{U_\infty}{\sqrt{gh}} \tag{2.2}$$

Here, g represents the gravitational acceleration, which decreases as the water depth increases. Given that Fr_h has been demonstrated to impact turbine hydrodynamics [15], it is essential to maintain it as a constant by adjusting U_∞ in all cases.

Additionally, the Reynolds number has been shown to influence turbine performance [16], and it is defined as:

$$Re_D = \frac{U_\infty D}{\nu}. \tag{2.3}$$

Here, ν denotes the kinematic viscosity. As U_∞ is adjusted to maintain Fr_h as a constant, Re_D must be kept the same by altering ν through the water temperature T. The values of $\lambda = 2.6$, 2.9, and 3.6 correspond to the respective peak power performance in Fig 2.4 for $\beta = 35\%$, 45%, and 55%, which were selected for further analysis.

2.3 Particle Image Velocimetry Data Image Acquisition setup

A two-camera, three-velocity component stereo PIV system was utilized to measure velocities within various cross-flume planes, as depicted in Fig. 2.5. Positioned perpendicular to the surface of water-filled prisms, two sCMOS high-speed cameras minimize distortion caused by refraction when light transitions between different mediums. Given the assumed symmetry of flow about the array center plane, the Field of View (FoV) of both cameras is solely directed toward the domain center behind Turbine B, as shown in Fig. 2.2. Following this adjustment, each camera adopts a slightly different angle of incidence close to 45 degrees to the image plane, resulting in an overlapping region measuring 42.3×27.7 cm^2. Any

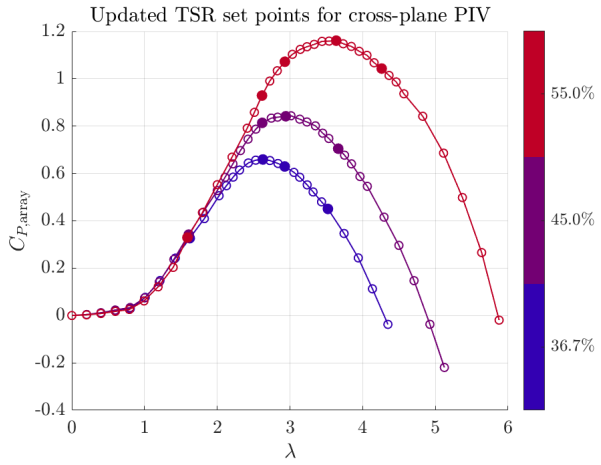

Figure 2.4: CFT array's coefficient of power C_P as a function of λ for $\beta = 35\%$, 45%, and 55%

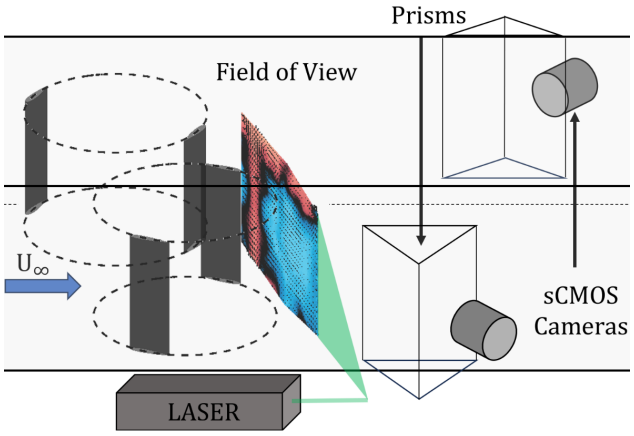

Figure 2.5: PIV image acquisition schematic with scale turbine and example flow field data.[1]

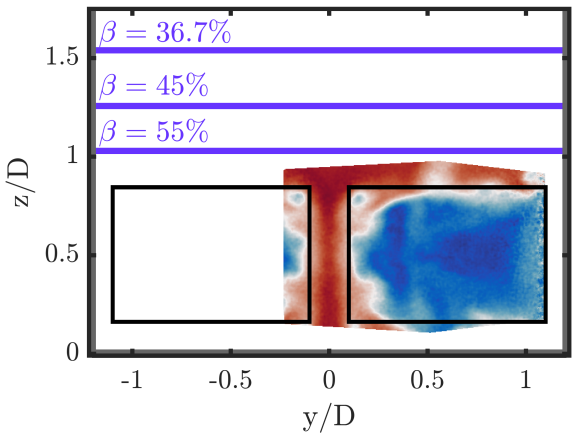

Figure 2.6: The PIV field of view (FoV) is positioned within the flume, as illustrated in the diagram. The black rectangles delineate the projected areas of the turbines, while the blue lines indicate the nominal location of the free surface at each blockage.

remaining focal length distortions within this FoV are effectively corrected and minimized using Scheimpflug camera lens adaptors.

The FoV is strategically positioned 5.2 cm above the flume bottom and 6 cm from the acrylic wall to maximize captured flow while mitigating overexposure regions caused by laser scattering due to wall presence in the test section. Consequently, the resulting FoV encompasses the entire projected region of one turbine, along with the bypass regions at the array center and atop the focused turbine.

The calibration process, facilitated by a dual-plane calibration target, enabled the conversion of camera images from pixel to physical space. This calibration data were then integrated into the PIV cross-correlation process, yielding a scale factor of 7.97 pix/min between the cameras. The fitting error for the two cameras was recorded as 0.81 and 0.92 pixels, respectively.

Neutral buoyant hollow glass spheres, each with a diameter of 10 μm, are uniformly dispersed throughout the flow. These spheres serve to trace the local fluid motion and are illuminated by a light sheet approximately 2 mm thick. The light sheet is produced using a

dual pulse 200 mJ Quantel Evergreen Nd:YAG laser, fitted with a -20 mm cylindrical lens.

Velocity data were collected at three cross-flume planes positioned at 0.6D, 1.0D, and 1.5D downstream of the turbine streamwise center during the experiment. These planes were denoted as the 0.6D, 1.0D, and 1.5D planes, respectively, for subsequent analysis. At each location, the turbine array was translated in the streamwise direction, while the laser light sheet and cameras remained stationary. Data acquisition was synchronized with the turbine blade angle (θ) for every 3° phase angle increment in each condition. Given the turbine's dual-blade configuration, phase angles from 0 to 177° were recorded. A total of 400 frames were captured for each phase angle, resulting in 24,000 frames for each location and 120,000 frames for each β. Phase-averaged fields were generated by averaging the 400 frames corresponding to a specific θ, while time-averaged fields were created by averaging all 60 phases at the same x location in each condition.

2.4 Particle Image Velocimetry Data Processing

All recorded PIV data were processed using LaVision Davis 10.2.1 software. The software's stereo self-calibration function corrected any minor misalignment in the system. The raw image pre-processing pipeline includes a minimum filter to subtract the image background and a non-linear high-pass filter, which utilizes an average polynomial fit with an 11x11 pixels interrogation window, to mitigate unsteady laser reflections from the blade and free surface. Vector calculation begins with an initial 128x128 interrogation window with 50% overlap, followed by four subsequent passes that reduce to a 32x32 window and 75% overlaps. PIV vector validation only passed velocity vectors with a stereo reconstruction error of less than one pixel. Following PIV calculation, vector post-processing involves three passes of a universal outlier detection median filter[17], removing vectors with a signal-to-noise ratio of more than 1.5 but reinstating them if less than 2.5 for a 7x7 domain. The processed flow field from PIV was imported into Matlab for visualization and further analysis.

Due to the substantial volume of high-resolution images, totaling approximately 10TB of storage, required for this experiment, conducting all PIV processing on a single local

computer proved to be prohibitively time-consuming. To address this challenge, the data sets were divided into smaller groups and uploaded to the Hyak cluster, a scientific HPC at the University of Washington. Utilizing the cluster's capabilities, the data groups were distributed to multiple nodes and processed using LaVision DaVis-generated processing scripts, compressing months of processing time into just a few weeks. The author dedicated weeks to installing all necessary software and optimizing processes on the cluster, meticulously documenting each step with well-structured instructions for future reference. This cluster-based processing significantly improved the feasibility of large-scale PIV analysis and alleviated the arduous nature of the process, enabling the research group to study a wider range of turbine flow conditions with high spatial resolution more efficiently in the future.

In the processed PIV flow field, U_x, U_y, and U_z represent the velocities in the streamwise (x), lateral (y), and vertical (z) directions, respectively. Vorticity is calculated with a central difference scheme and its components will be denoted as ω_x, ω_y, and ω_z. Notably, ω_x is often termed in-plane vorticity because it is derived from the in-plane velocities within the recorded data planes. In all planar figures, the x-axis is oriented into the page, with the z-axis pointing upwards, necessitating the y-axis to point to the left. These conventions maintain consistency and clarity throughout the spatial analysis within this study.

Chapter 3

EXTRAPOLATING 2D FIELDS INTO A 3D VOLUME ASSUMING A FROZEN FLOW HYPOTHESIS

3.1 Frozen flow Hypothesis

A methodology to reconstruct the three-dimensional volumetric flow field is proposed to better assess the complex three-dimensional flow structures in the wake of the CFT array. This method utilizes the three cross-planes of stereo PIV data at x/D=0.6,1,1.5. We utilize Taylor's frozen flow hypothesis, which posits that the flow maintains its velocity profile and does not evolve as it is convected downstream. In other words, the flow does not experience changes in its structure due to effects such as diffusion or external forces; it merely translates along the streamwise direction. Assuming it is valid for this application, the velocity profile in each recorded frame can be assumed to be "frozen" and the convection of this profile by the fluid can be estimated as a translation to a downstream position.

As mentioned before, θ is the phase angle of the turbine, which establishes a temporal reference frame linked to the rotation of the turbine. For clarity, let θ_f be the phase angle of the particular field we are translating. Based on the frozen flow hypothesis, planar fields for all θ_f and at all three data planes (x/D=0.6,1,1.5) could each be placed at an appropriate streamwise location to reconstruct and interpolate the full volumetric field. The convected streamwise location x_c of the field for a given θ_f can be estimated by

$$x_c(\theta_f, \Delta t) = x_0 + U_{cAvg}(\theta_f)\Delta t, \tag{3.1}$$

here x_0 is the streamwise position of the data plane where the field is captured, U_{cAvg} denotes the average convective velocity within the interval between the data planes through which

the field is convecting, and Δt is defined as

$$\Delta t = \Delta\theta \frac{dt}{d\theta} \tag{3.2}$$

represents the duration for the flow to convect the field. In this case, $\Delta\theta$ is given as

$$\Delta\theta = \theta_f - \theta \tag{3.3}$$

When $\theta_f = \theta$, the field is located at the data plane where it was captured. Since the flow field changes with turbine rotation, U_{cAvg} is a function of θ_f. As the PIV setup records flow field data at a constant rate, $\frac{dt}{d\theta}$ denotes the time per degree of turbine rotation and remains constant for a given condition. For example, to determine the x_c of the field at $\theta_f = 30°$ when the turbine is at $\theta = 0°$ and $\beta = 55\%$, we first calculate Δt using Eqn 3.2 and then apply it, along with the U_{cAvg} calculated by method in the next section, to Eqn 3.1. Utilizing these relationships, all field data collected at a constant streamwise position can be transformed into spatial data at a fixed time.

3.2 Determining the most appropriate convective velocity

Key to the proposed approach to three-dimensional flow reconstruction is our ability to estimate a convective velocity that yields a good average representation of the flow structure. Due to power extraction, the turbine harvests part of the momentum in the flow to generate torque, resulting in a lower flow speed behind it. Thus, utilizing the free stream velocity is not a suitable estimate of the convective velocity in the turbine wake. A better estimation is to use the average streamwise velocity evaluated in each field at θ_f as the $U_c(\theta_f)$ and assume it is constant during the convection. However, U_c does not stay as a constant in all streamwise locations and the average velocity calculated also depends heavily on the field of view. Hence, a method to estimate the convective velocity and capture its variation in space by correlating flow structures between frames at successive streamwise measurement locations is preferred.

To best determine the convective velocity of dominant flow structures, we correlate the in-plane vorticity fields between the turbine cross-stream flow fields. It is assumed that the

dominant flow structures within the turbine wake are all being convected at the same speed (the validity of this assumption will be addressed later) and that this speed is dependent on the phase of the field θ_f. For a given turbine θ, the in-plane vorticity (calculated with central difference scheme) of the respective $\theta_f = \theta$ frame at an upstream location, denoted as θ_{f1}, is correlated with all θ frames at the next downstream location, denoted as θ_{f2}. The vorticity data is initially mapped onto a standardized grid to ensure uniformity in the size of vorticity fields across the dataset. Subsequently, the mapped data are converted into a column vector format. Let the column vector for the vorticity field at the upstream location be x_a and that at the downstream location be y_b. The Spearman's rho correlation [18] coefficient is calculated as,

$$r_s = 1 - \frac{6 \sum d_i^2}{n(n^2 - 1)}, \tag{3.4}$$

where d_i is the difference between the ranks of the two columns, and n is the length of each column vector. Spearman correlation was selected over Pearson correlation due to its less stringent nature, as it does not assume a normal distribution, which cannot be inferred in this particular application.

Once an upstream frame for a particular θ is correlated with all frames from the next downstream position, the variation in correlation coefficient with $\Delta\theta$ can be examined in the correlation profile as shown in Fig3.1. The $\Delta\theta$ is defined as

$$\Delta\theta = \theta_{f2} - \theta_{f1}. \tag{3.5}$$

The range of $\Delta\theta$ spans from 0 to 360 degrees because the upstream field may require a full turbine revolution to reach the downstream plane. To enhance stability in identifying the correlation peak, a Gaussian filter with a width of 20 data points is applied to the correlation profile. This filtered correlation peak denotes the time it takes (calculated by applying θ_{f2} as θ_f and $\theta_{f1} = \theta$ in Eqn 3.2) for the upstream θ_{f1} field to convect between the planes. Utilizing the known distance between the two locations, U_{cAvg} is estimated by dividing this distance by the time. This process is iterated for all θ_f at the upstream plane to capture the variation of $U_{cAvg}(\theta_f)$ with θ_f. In this sense, $U_{cAvg}(\theta_f)$ represents the average convective velocity for

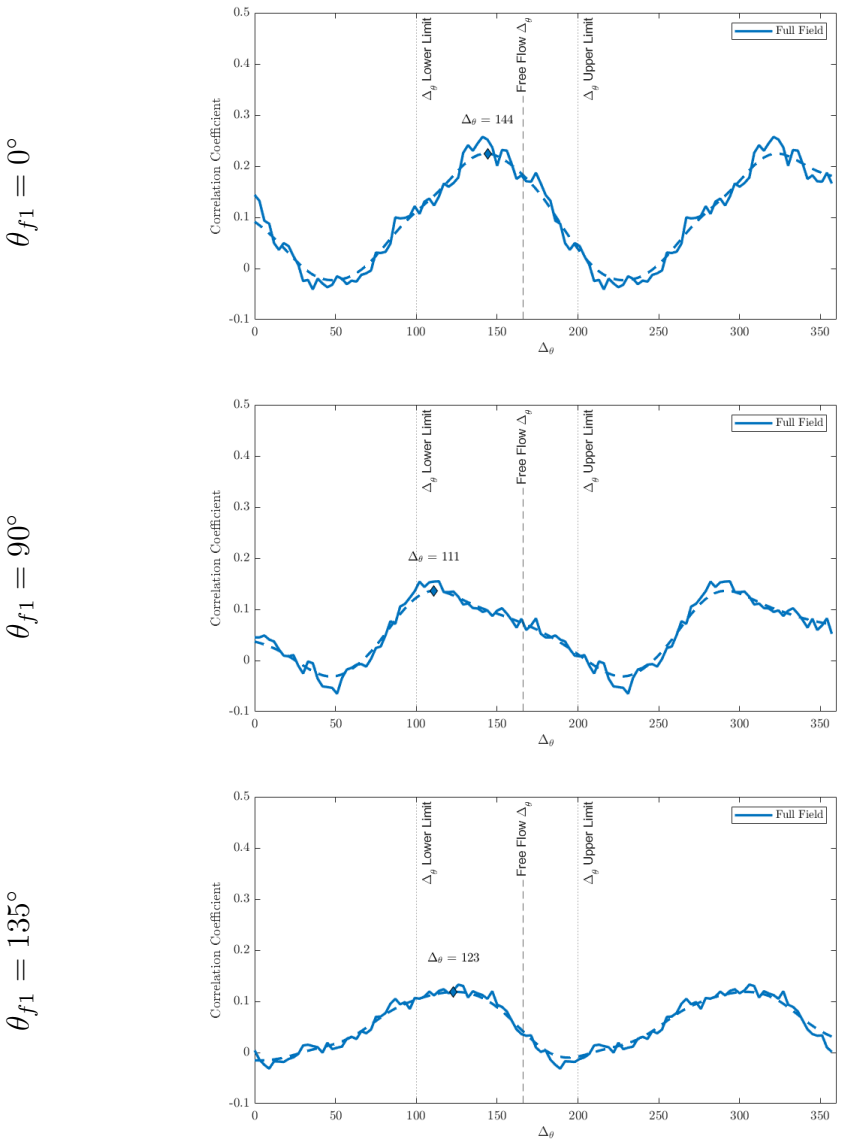

Figure 3.1: Example correlation profile. ω_x field at 0.6D downstream for $\theta_{f1} = 0,\ 90,\ 135°$ is correlated with ω_x fields for all θ at 1.0D downstream $\beta = 55\%$. The free flow $\Delta\theta$ corresponds to the time it takes for the field to reach the downstream plane if $U_{cAvg} = U_\infty$. Since the profile is periodic, the upper and lower limit range is set to capture the peak that is located near the free flow Δ_θ

an upstream field with θ_f within the interval between the two correlated data planes.

The in-plane vorticity ω_x was chosen for the analysis because its correlation profile peak is much more distinct and stable than others ($U_x,\ U_y,\ U_z,\ |U|$). As shown in Fig 3.1, the correlation profile varies with θ_f but always retains a single prominent peak in a single period. Since this paper aims to investigate the fluid structures in the wake region, utilizing vorticity would provide a more insightful indication of how the vortex structure evolves.

3.3 Estimating the streamwise evolution of convective velocity

Eqn 3.1 assumes that the flow is convected at a constant speed within the interval between the two correlated data planes. However, the convective velocity experiences significant deceleration from 0.6D to 1.5D downstream. To account for the changes in convective velocity $U_c(\theta_f)$ with streamwise location, we utilize the following equation

$$x_c(\theta_f, \Delta t) = x_0 + \int_0^{\Delta t} U_c(\theta_f, x)\, dt, \tag{3.6}$$

where U_c is the convective velocity that is a function of x for a given θ_f. The integral can be solved explicitly or numerically once the function U_c is determined.

After correlating a particular θ_{f1} field at the 0.6D plane with all fields in the 1.0D plane, a θ field corresponding to the correlation peak at 1.0D, noted as θ_{f2}, and the averaged convective velocity in this interval, noted as U_{cAvg1}, can be calculated. Then, the θ_{f2} field at 1.0D is used again to correlate with all fields at 1.5D to find θ_{f3} and U_{cAvg2} similarly. According to the frozen flow hypothesis, fields for θ_{f1}, θ_{f2}, and θ_{f3} at 0.6D, 1.0D, and 1.5D planes, respectively, all represent the same field but are translated snapshots captured at different data planes. Consequently, U_{cAvg1} and U_{cAvg2} represent the averaged convective velocity for the 0.6D θ_{f1} field between the 0.6D to 1.0D and 1.0D to 1.5D intervals. To estimate the variation of $U_c(\theta_{f1},\ x)$ in x, linear interpolation can be used as shown in Fig 3.2.

Realistically, $U_c(\theta_f,\ x)$ is likely to be nonlinear for x. However, since the experiment only collected data at three different downstream planes, resulting in only two data points

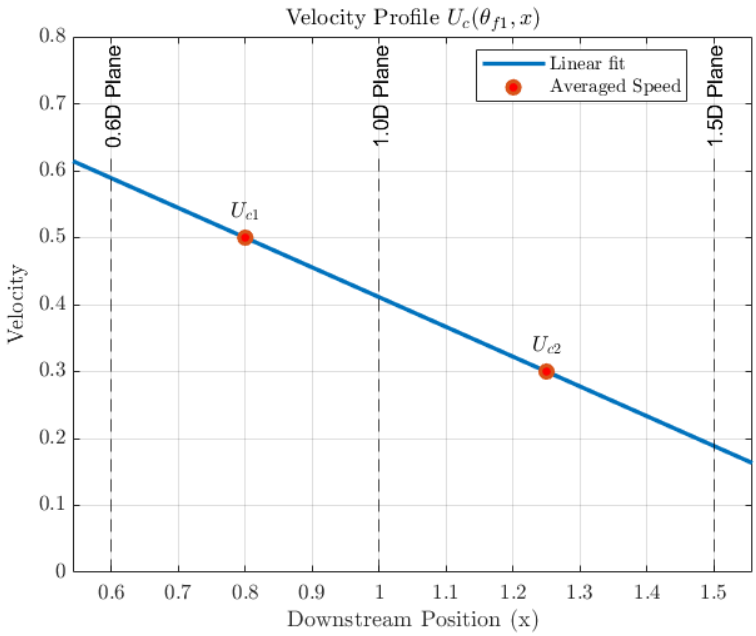

Figure 3.2: The interpolation of convective velocity involves placing U_{cAvg1} and U_{cAvg2} at the center of their respective intervals to ensure they represent the averaged value within each interval.

available for interpolation, linear interpolation is chosen for the analysis in this study. It's worth noting that this approach may lead to underestimation of the convective speed in certain domains and overestimation in others.

3.4 Reconstruction of flow in space and time

While the reconstruction method is based on the frozen flow hypothesis, it's important to recognize that fluid structures are likely to deform and evolve between data planes due to turbine induction and mixing between flow regions. To approximate the streamwise evolution, we utilize a weighted average of the flow field estimates between known data planes. This allows us to reconstruct a coherent volumetric flow field that best estimates the true three-dimensional fluid field spanning from 0.6D to 1.5D.

To create the flow field estimate from a selected data plane for a given turbine θ, all θ_f fields acquired from this data plane are placed at their respective x_c found by using $U_c(\theta_f,\ x)$ for the respective θ_f into Eqn 3.6 in which $\Delta\theta$ is calculated from Eqn 3.3 and Δt is calculated from Eqn 3.2. This flow field estimate can also extend in the direction upstream of the data plane by specifying Δt as a negative value. Since θ_f is periodic, this can be achieved by setting θ_f to be the equivalent angle that is one or multiple periods apart from it. Moreover, this periodic estimation can extend as far as possible by setting θ_f equal to its equivalent angles, ensuring the flow field estimate from a data plane can at least extend to the subsequent data plane. During the reconstruction, four different flow field estimates are calculated for each β: two extending downstream from 0.6D and 1.0D planes, and two extending upstream from 1.0D and 1.5D planes. Each estimate extends to the next data plane in the respective direction. The largest distance between adjacent θ_f fields is less than $0.01D$ for all cases, with an average distance of around $0.005D$.

To simulate the evolution of the flow field between data planes, the four flow field estimates are blended with a weight function with the estimate that spans the same interval to construct a single coherent volumetric field for a given θ and β. Before blending, each estimated flow field is interpolated onto a common grid with a streamwise resolution of

$dx = 0.01D$ to allow matrix summation with the same size during the blending. The region extending from 0.6D to 1.0D downstream will be designated as the forward section, while the region from 1.0D to 1.5D downstream will be referred to as the aft section.

Because the flow field estimate is perfectly accurate at the plane where data are acquired and becomes increasingly less accurate further away from it due to flow evolution, the weight function is defined to be a function of x, namely $W(x)$. Its profile is defined to be a probability density function (PDF) given by:

$$W(x) = \frac{1}{\sigma\sqrt{2\pi}} \exp\left(-\frac{(x-\mu)^2}{2\sigma^2}\right), \tag{3.7}$$

where μ is the mean and σ is the standard deviation. For a particular flow field estimate, μ is evaluated to the x of the data acquisition plane, and σ is set to equal a third of the streamwise span of the flow field estimate. These values ensure that the weight is the highest at the original data plane and gradually decreases to a minuscule value at the next data plane. During the blending process, the weight function for each flow field estimate is weighted again to ensure that their sum is equal to one at all x to avoid biasing the result. The weight profiles are shown in Fig 3.3. The effect of blending is illustrated by the example in Fig 3.4. The blended field shows a smooth transition between the two extrusions. The area closer to $0.6D$ shows a higher resemblance to the 0.6D downstream extrusion and the $1.0D$ area is more similar to the 1.0D upstream extrusion.

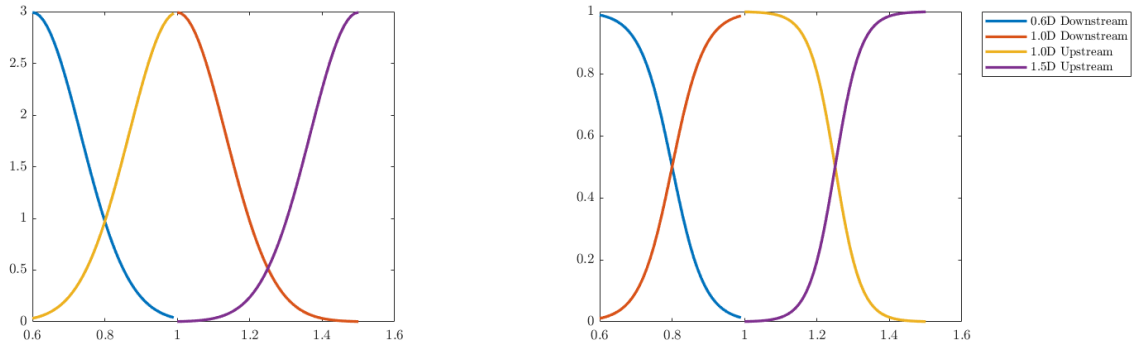

Figure 3.3: Weight function for each extrusion. "0.6D Downstream" denotes the flow field estimate moving downstream from the 0.6D plane. The left side illustrates the probability density function (pdf) for each estimate, while the right side displays the final weighted function, ensuring their sum equals one.

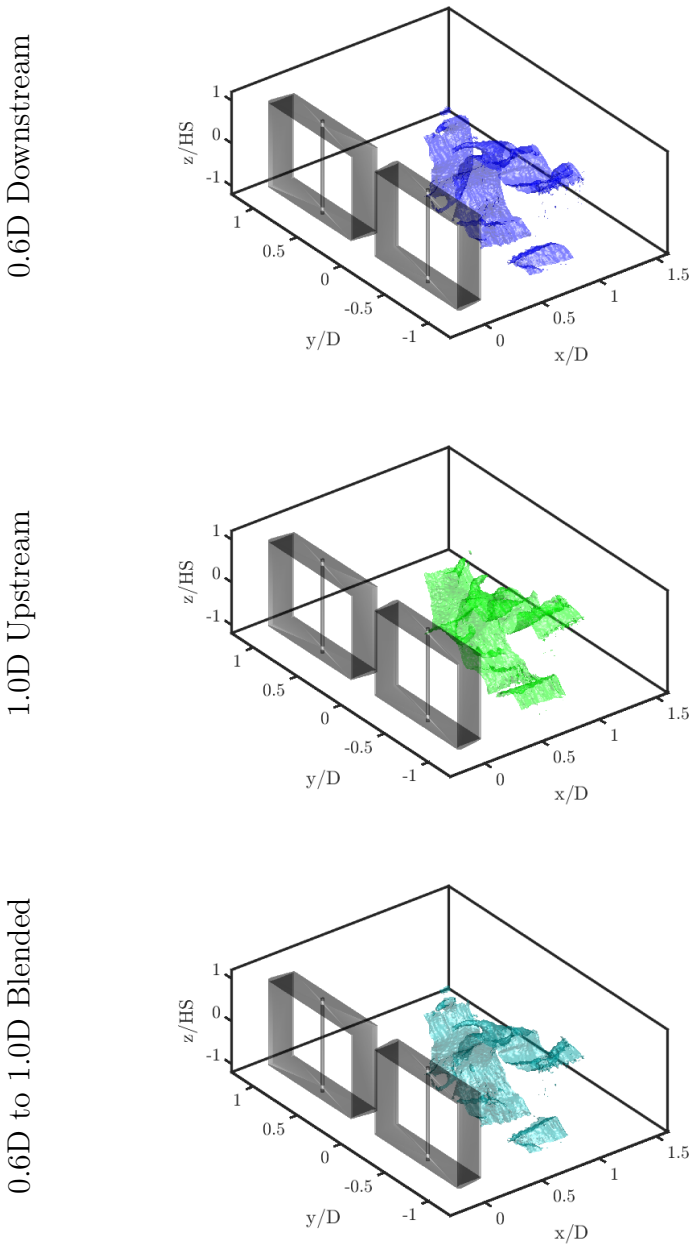

Figure 3.4: Example to show the blending of the estimate to create the final reconstruction between 0.6D and 1.0D for $\beta = 55\%$ $\theta = 0°$. The isosurface shows $U = U_\infty$.

Chapter 4

RESULTS AND DISCUSSION

As mentioned in Section 2.2, this work investigates the cases at $\beta = 35\%$, 45%, and 55% with respective peak power $\lambda = 2.6$, $\lambda = 2.9$, and $\lambda = 3.6$. It is also important to note that since the phase offset of the two turbines is zero, the symmetry of the flow behind them should be expected.

4.1 Time Averaged Flow Field

The 3D rendering of the averaged flow velocity within each PIV domain is shown in Fig 4.1. The $\beta = 55\%$ confinement case is selected to highlight the flow field under the highest blockage, where the strongest flow gradients are expected. Data are shown for the right-hand side of the center plane (looking downstream in the flume); however, this is sufficient to describe the entire flow due to symmetry. The planar stereo (PIV) field data will be categorized within the following sections to facilitate precise location references. The term "wake region" pertains to the region encapsulated by the rectangle that outlines the projection of the turbine, as depicted in Fig 2.3. Conversely, the "bypass region" denotes the space surrounding the wake. Within the bypass region, the "center bypass" encompasses the rectangular region between the two wake areas, including the zones above and below the vertical span of the turbines. The areas directly above and below the wake are referred to as the "top bypass" and "bottom bypass", respectively. The "sidewall" denotes the vertical flume boundary situated to the right of the wake.

In Fig 4.1, the wake appears to extends behind the turbine for many diameters, gradually weakening. Outside the slow-moving wake, in the bypass region, the flow is accelerated due to induction. A distinct boundary between these two regions can be identified as the white band,

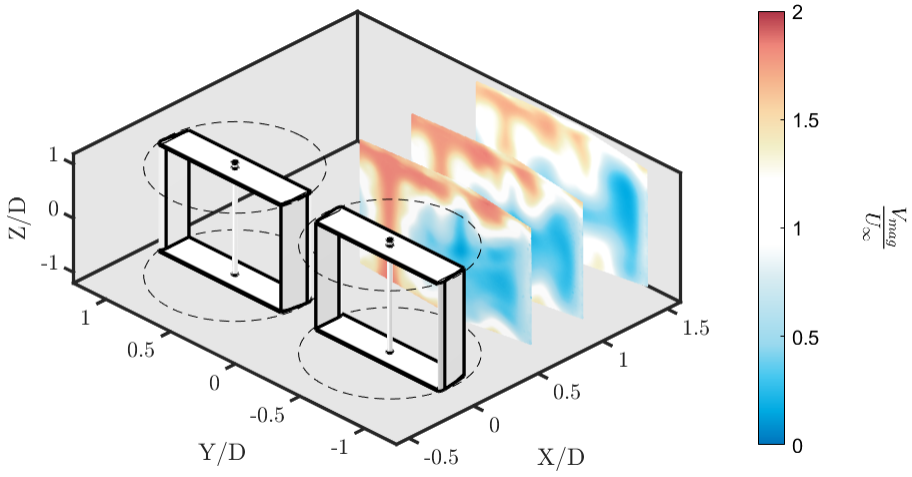

Figure 4.1: Time averaged flow fields acquired and their relative locations to the turbine. $\beta = 55\%$ with planes at 0.6, 1.0, and 1.5D downstream from the turbine center. The dashed circle outlines the range of motion of the turbine blade

in this case selected to be $|U| = U_\infty$, as illustrated in the figure. Noticeable developments and evolution are observed in all regions as the flow progresses downstream.

The influence of confinement on the evolution of the time-averaged turbine wake at each of the downstream stations is explored in Figure Fig. 4.2. The z-axis of the figure is scaled in terms of the half span (HS) of the turbine blade. In contrast to Fig 4.1, the color map depicts the streamwise component, while the vectors represent the in-plane components. To enhance visualization, the vector fields are down-sampled by a factor of ten onto a common grid, and their scale is kept consistent across all figures to enable direct comparison. Within the observable range of the mean field, the flow appears symmetric about the vertical centerline of the center bypass, supporting the assumption that the flows behind the two turbines are similar.

Looking at the general profile of the flow field, it is observed that there is a high-velocity flow in the bypass and a slower flow in the wake, directly behind the turbine (shown in

blue). The horizontal center of the wake flow prominently exhibits lateral velocity towards the right in all cases. This lateral motion can be attributed to the rotating turbine blades imparting lateral velocities to the flow. When the aft cycle ($\theta = 180 - 360°$) blade moves to the right, the flow is expected to follow it in the same direction. The top and bottom of the wake are dominated by the flow that entrains momentum from the bypass region. The top and bottom of the bypass region exhibit fluid moving away from the mid-span of the turbine blades.

As β increases, the velocity (U) in the bypass flow exhibits a significant rise, whereas the velocity in the wake region is less affected. The velocity profile (U) in both bypass and wake flows becomes less uniform, and their shapes change significantly as blockage increases from $\beta = 45\%$ to $\beta = 55\%$. At 1.5D downstream, the size and shape of the wake flow for $\beta = 55\%$ show a distinct difference compared to lower blockages.

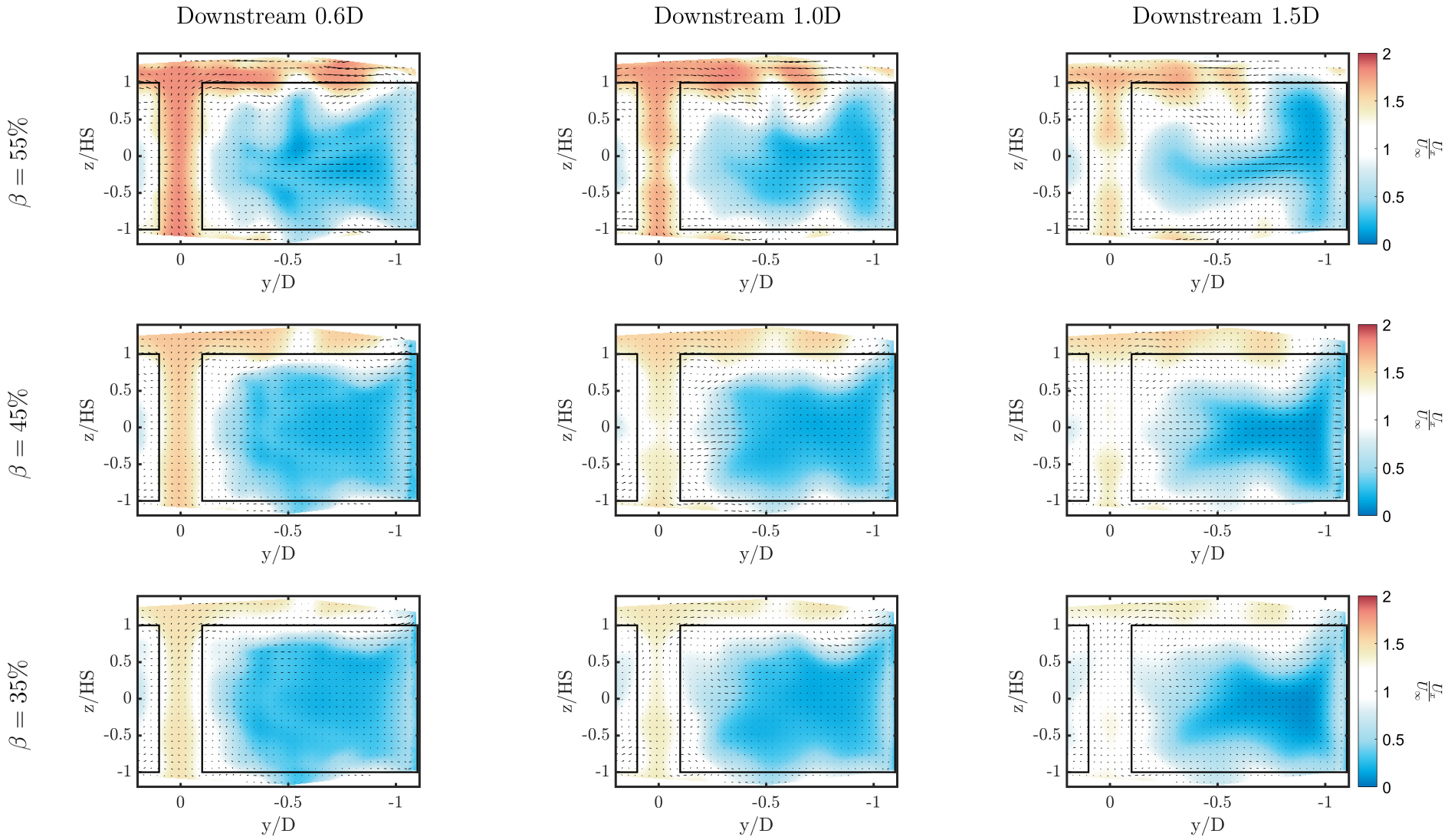

Figure 4.2: The time-averaged velocity fields at different x location and β

When the flow is convected downstream, the peak bypass velocity decreases. In contrast, the wake appears to narrow, but its minimum velocity does not change significantly. Despite a rapid decrease in U for the entire domain, the in-plane velocities (V and W) remain high at 1.0D and 1.5D, particularly for $\beta = 55\%$. As the flow moves downstream, the wake region shrinks but shows a higher concentration of slow flow at its center. The transition area marked by $|U| = U_\infty$ expands in later downstream locations. This is expected due to momentum transfer across the shear layer between these regions, resulting in a reduced size of both the bypass and wake and an expanded transition area between the two.

In the observed fields, both the wake and bypass regions exhibit top and bottom symmetry. Interestingly, the symmetry plane appears to shift downward in the later downstream positions, suggesting a downwash due to external influences. By defining the wake's horizontal centerline as the line with the minimal vertical velocity component, it becomes evident that this centerline descends and deviates from straight as the flow progresses downstream. This deviation implies that the flow isn't strictly two-dimensional. Even at the turbine midspan plane, three-dimensional fluid structures may still influence the flow. One potential factor contributing to the observed downward shift is the downwash effect, which occurs as the turbine converts some of the flow's kinetic energy into mechanical energy. This energy conversion typically causes a drop in the free surface of the water, resulting in a downwash behind and above the turbine. Additionally, the proximity of the bottom bypass region to the floor may also play a role. Here, the boundary layer and surrounding hardware could dampen vortex activity, further disrupting the symmetry between the top and bottom flows.

4.2 Phase-Averaged Flow Fields

To explore the coherent structure of the turbine wake implied by the time-averaged fields, Fig 4.3 introduces the phase-averaged variation of velocities and in-plane vorticity, ω_x (with positive values pointing into the page) at a distance 0.6D downstream of the turbine axes. Phases are limited to between 0 and 180° due to the use of a two-bladed turbine. Once again, the highest confinement case is highlighted. Phase-averaging of 40 frames has been

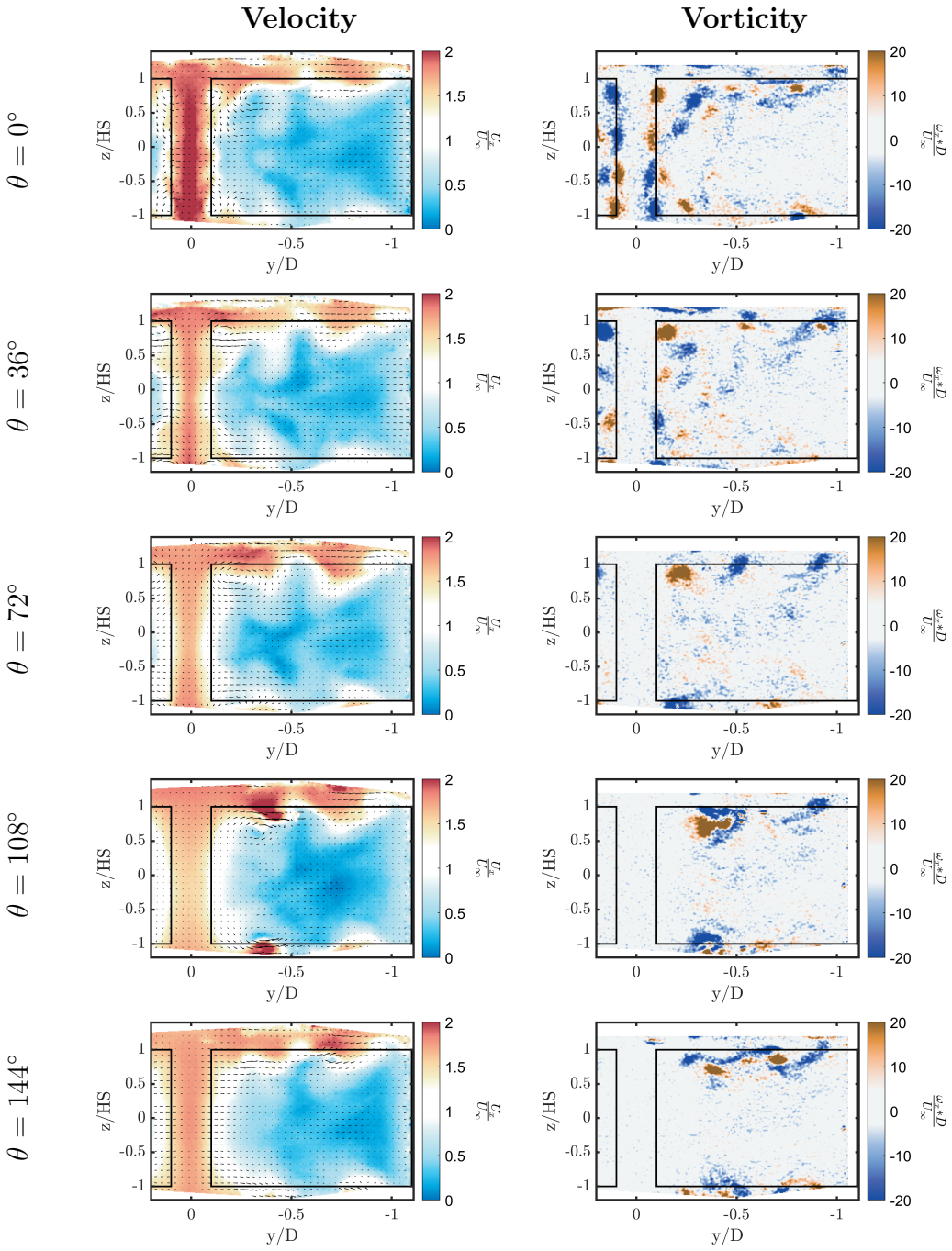

Figure 4.3: The (left) Velocity field and (right) Vorticity field for a few selected θ at $\beta = 55\%$ at 0.6D plane

used to produce these figures. While this reduces the noise and cycle-to-cycle variation of the results, some noise remains in regions close to the flume side wall and the free surface due to challenging reflections that could not be fully eliminated during PIV processing. These areas are cropped out of the vorticity fields due to the greater sensitivity of this metric to noise. The cropped section is a rectangle with a width of $0.02D$.

Several interesting features are observed in the flow as the blade θ changes. There is a well-defined plane of symmetry at the mid-span for all θ. The maximum bypass velocity occurs when the blades sweep through their closest approach at $\theta = 0°$ as expected. Maximum velocities otherwise are also observed near the strong vortex cores. Prominent tip vortices appear at the top and bottom corners of the turbine at $\theta = 0°$ and move in the wake of the turbine as the blade continues to rotate, contributing to the overall flow dynamics. There is an interesting interaction of vorticity near the phases of maximum bypass velocity. Additionally, the top and bottom surfaces of the slower wake flow appear to deform inward, suggesting strong local entrainment from the bypass region. These features will be expanded upon with greater detail in the following paragraphs:

Similar to observed in the time-averaged field in Fig 4.2, the fluid behind the two turbines appears symmetrical about the flume's longitudinal centerline across all θ. The two wake regions are relatively separated and there is no direct momentum transfer between the two wakes. There is also a symmetry about the mid-span plane, and there is little to no vertical velocity on this plane, especially in the bypass region. Consistent with observations made in the averaged fields, the symmetry plane is positioned lower than the mid-span of the turbine.

The bypass flow exhibits its highest velocity at $\theta = 0°$ and its lowest velocity near $\theta = 90°$, due to the convergence of the two blades at $\theta = 180°$, which compresses the flow forward, creating a small region of high velocity, referred to as a high-velocity burst.

At all θ values, the locations of the four prominent tip vortices exhibit almost four-way antisymmetry. They are generated at around $\theta = 0°$ and are easily observable near the top and bottom bypass side corners of each turbine during $\theta = 0 - 90°$. These vortices resemble those generated by a three-dimensional wing in a steady flow, suggesting that the

lift distribution on the turbine blade is likely non-uniform across the span with the highest lift occurring at the blade's mid-span. The resulting pressure differential may drive the vertical movement in the center bypass region, where the flow diverges from the turbine mid-span and moves upward and downward.

Notably, the tip vortex at the top left corner of the wake region rotates clockwise, as the pressure side of the blade is on the outboard surface, which is consistent with previous findings [8]. These tip vortices are expected to be significantly stronger than those generated by the same blade in static flow due to dynamic stall and the combined high pressure from the two blades. Dynamic stall phenomena are well-documented for CFT turbine blades [8] and result from rapid changes in the blade's angle of attack (AOA) due to rotation. This leads to the formation of large leading-edge vortices (LEV) that temporarily increase the blade's coefficient of lift before the LEV detaches and the blade stalls. The high lift during dynamic stall causes a substantial pressure difference across the blade, contributing to the formation of larger tip vortices. As the blades approach $\theta = 180°$ and come into proximity, the merging high-pressure regions significantly increase the pressure difference across each blade, further enhancing the strength of tip vortices. As θ increases, the tip vortices move right, likely due to their attachment to the blade and movement along with it. Further analysis suggests that these tip vortices play a crucial role in forming other vortex structures and transferring momentum between different flow regions.

At $\theta = 170°$, just before the high-velocity burst reaches the 0.6D data plane, flow near the mid-span is pushed away from the bypass into the wake, resulting in a high lateral component while flow at the top remains relatively unaffected. This differential in flow speed may contribute to the formation of vortices at the top and bottom corners of the wake region near the tip vortices. These can be best observed at $\theta = 0$ & $36°$. Following the passage of the high-speed flow, pressure in the bypass decreases, causing fluid from the wake to move toward its center. As a result, these vortices disappear when the speed differential that drove them ceases to exist.

At $\theta = 0°$, an interesting cross pattern appears at the mid-span of the turbine, and its

formation appears to be closely linked to the in-plane velocity. The tip vortices are the strongest at this θ, and they induce high-flow entrainment from both the top and bottom bypass into the wake region. The entrained flows from these vortices exhibit nearly identical vertical velocity magnitudes. Upon the entrained velocity merging at the mid-span plane of the turbine, a horizontal line with minimal vertical velocity emerges. This plane acts as a virtual wall, and as vertically moving fluid approaches it, a stagnation point forms. This phenomenon is most pronounced at $\theta = 0°$, to the right of the vertical center of the bypass. As fluid approaches the stagnation point, it splits and moves to the left and right to maintain momentum conservation. This turning of fluid tends to cause viscosity-induced shearing between each streamline, contributing to vorticity generation. Specifically, fluid moving to the right gives rise to the blue vortex, while flow directed to the left forms the red vortex. Given the lower pressure in the bypass indicated by the in-plane velocity pointing into the center bypass from the wake, more fluid is drawn into this region upon exiting the stagnation point. As it enters the bypass, it is redirected vertically away from the center due to the uneven pressure distribution on the blade. Consequently, the vortex closer to the bypass (the red vortex) experiences a higher concentration of generated vorticity by the turning fluid. Due to the inherent symmetry of the flow in both the vertical and horizontal directions, this interaction occurs symmetrically across the centerline, resulting in the formation of four vortices comprising the cross pattern near the horizontal mid-plane at $\theta = 0$ & $36°$. Notably, the cross pattern dissipates rapidly after $\theta = 36°$, coinciding with the attenuation of the flow pattern that may be responsible for its generation.

As the β level decreases, the cross pattern appears distorted. This distortion occurs because the tip vortices become less concentrated in lower β and their vorticity is distributed over a larger area. As a result, the larger tip vortex boundaries become closer to the cross pattern and exert velocity influences on the vortices within the pattern. Specifically, at $\beta = 35\%$, the induced velocity from the top tip vortices causes two vortices in the cross pattern to merge with the tip vortices.

The upper and bottom parts of the wake region are dominated by flow entrained from

the bypass, as suggested in the mean-field. In Fig 4.3, this region exhibits inward concave deformation with a stationary protrusion in the middle for all θ. Since the protrusion is longitudinally aligned with the turbine center shaft, it is believed to be caused by its wake. Consequently, the entrained flow is also divided into two groups by the center shaft wake. This division is marked by a low entrainment zone aligned with the center shaft's position with higher entrainment on each side. The wake top surface adjacent to the bypass exhibits higher recession from $\theta = 0-90°$, which is likely due to induction from the strong tip vortices.

The top bypass exhibits more negative vorticity than positive vorticity. In a video showing the continuous development of the flow as θ changes, the scattered blue vortices at $\theta = 0°$ consolidate into two distinct large eddies as shown in $\theta = 72°$ as the blade moves. One vortex positioned to the right near the wall remains present and almost stationary throughout the cycle. The other vortex seems to attach to the center shaft from $\theta = 0 - 108°$, growing in magnitude within this interval due to increased induction as the tip vortices approach. At $\theta = 108°$, the tip vortex follows the blade and moves near the center shaft vortex forming a counter-rotating vortex pair. This pair may induce strong velocities on each other, causing them to move closer together and interact. During this interaction, the vortices appear elongated due to the three-dimensional vortex component interaction. Once this interaction concludes, the tip vortex continues to move with the blade but with a much smaller magnitude. At $\theta = 144°$, a similar interaction occurs between the tip vortex and the other blue vortex near the wall.

Fig 4.4, 4.5, 4.6, and 4.7 enable the comparison of velocity and vorticity fields under all three β at a few selected θ. The color maps are set to the same normalized values to facilitate direct comparison between the cases with different β. As shown in Fig 4.4, the highest bypass velocity appears close to $\theta = 0°$ for all blockages, and its magnitude decreases as β decreases. The in-plane velocity profile is very similar for all β, and the magnitude scales with β. The lowest bypass velocity consistently appears at $\theta = 90°$ for all β, as shown in Fig 4.6. Vortex structures are very similar at different β at optimum λ, and the location of each vortex is very similar across the cases. The wake region has a shape close to a rectangle

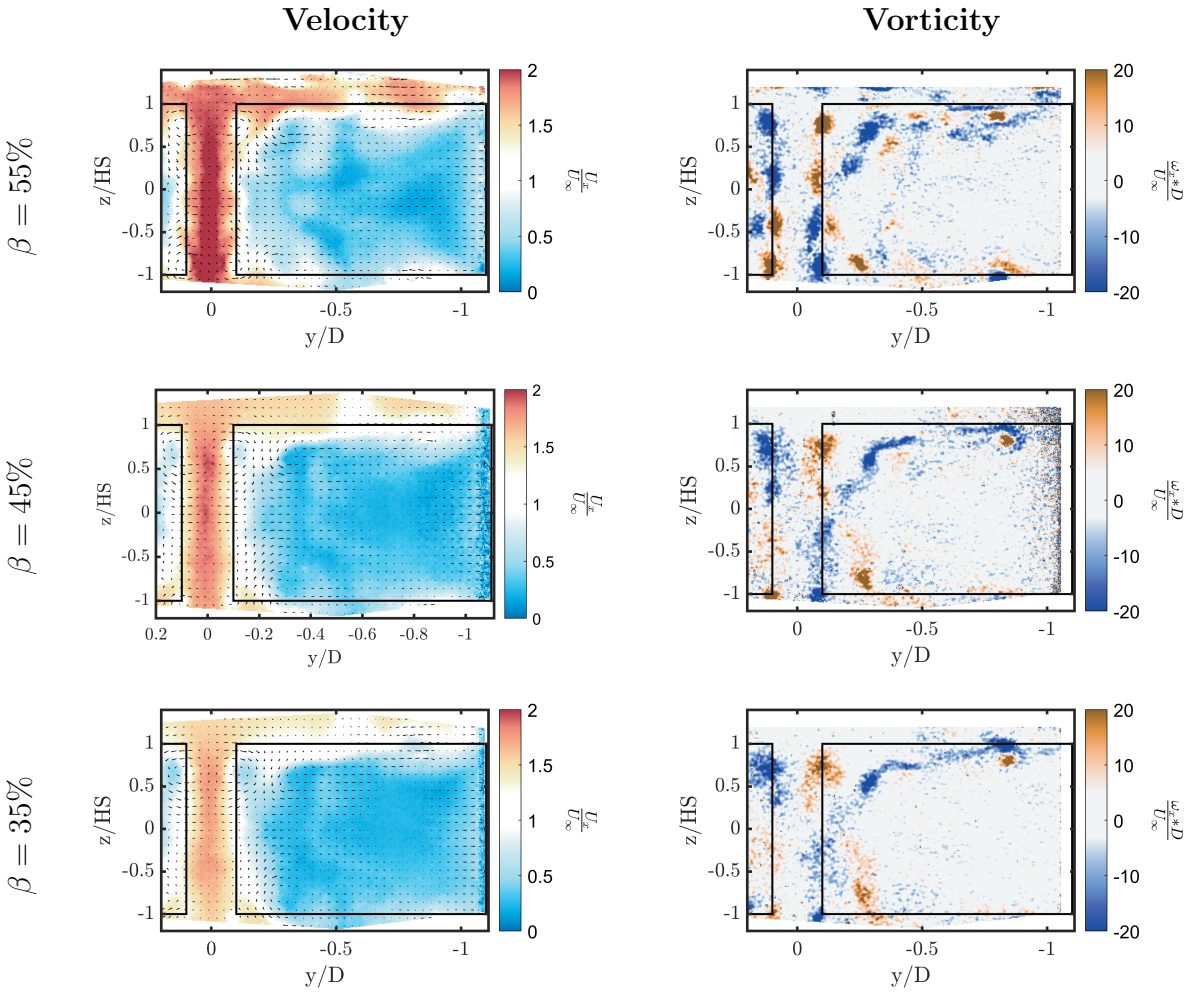

Figure 4.4: The (left) Velocity field and (right) vorticity field for $\theta = 0°$ at $0.6D$ Downstream

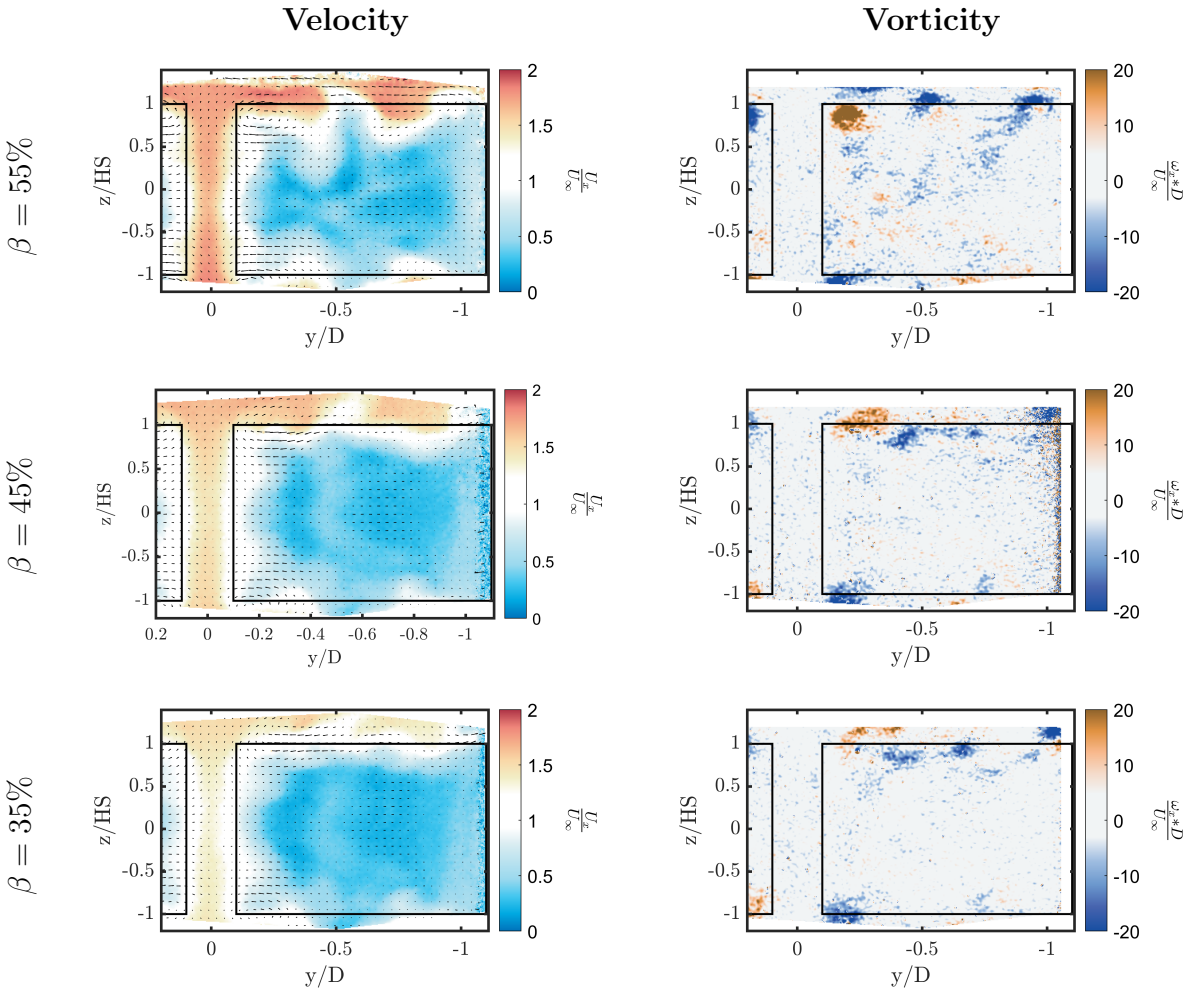

Figure 4.5: The (left) Velocity field and (right) vorticity field for $\theta = 60°$ at $0.6D$ Downstream

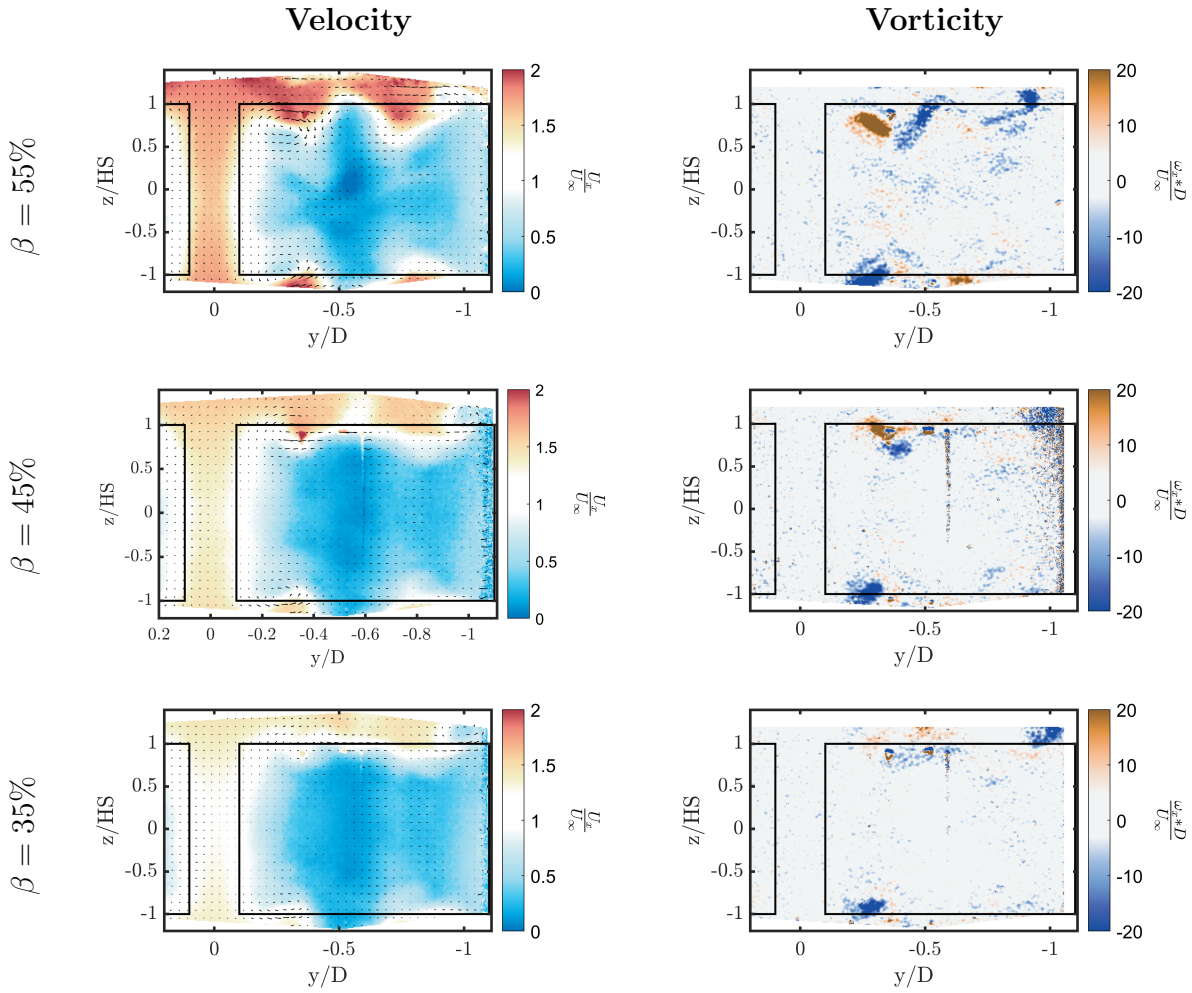

Figure 4.6: The (left) Velocity field and (right) vorticity field for $\theta = 90°$ at $0.6D$ Downstream

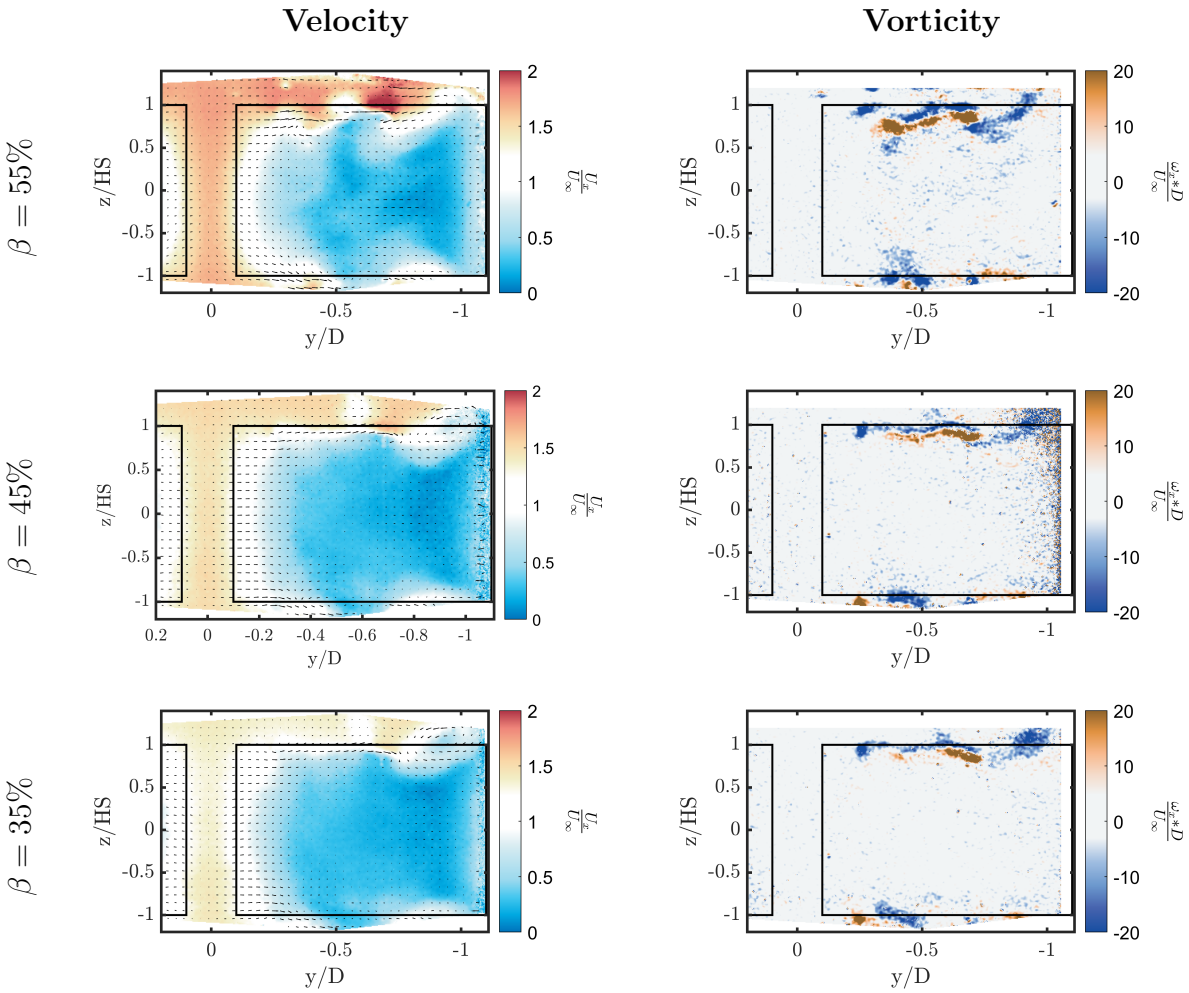

Figure 4.7: The (left) Velocity field and (right) vorticity field for $\theta = 135°$ at $0.6D$ Downstream

that fills the projection of the turbine at $\theta = 0°$. At other θ values, as shown in Fig 4.5, the wake deviates from this shape by exhibiting stronger entrainment from the bypass into the wake.

In lower β, the center shaft leaves a larger wake area behind it. This larger wake may dampen the vortex attached to the center shaft. At $\theta = 60°$ in Fig 4.5 the blue vortex in the top bypass breaks from one single vortex in $\beta = 55\%$ to several smaller vortices observed in $\beta = 45$ & 35%. Individual vortex also exhibits less concentration at lower β levels, as their blurry boundaries indicate. These vortices are also weaker and more dispersed across the full field. In turbulent flows, the viscous effects tend to become more significant when the eddy size is smaller, suggesting that vortex structures at lower β levels tend to dissipate more quickly.

A counter-rotating vortex pair would induce velocity on each other to move in the same direction. As they approach the wall, they split and move further away from each other. At lower β, the free surface that can act as the wall is further away from the turbine, allowing the tip vortices to travel higher up or lower down while they move sideways following the blade, as observed in Fig 4.4, 4.5, 4.6, and 4.7.

4.3 Best-Correlated Phase-Averaged Flow Field Pairs

Figure 4.8 and 4.9 display the best-correlated pairs determined by the correlation method introduced in Chapter 4.2 at $\theta = 0°$ and $90°$ respectively, when $\beta = 55\%$. The velocity and vorticity fields show a noticeable evolution as expected, yet the features in the most upstream fields remain well recognizable in all downstream fields, supporting the validity of the frozen flow hypothesis for this application. The correlation, calculated based on vorticity, effectively captures the variation in vortex structures at different θ. Furthermore, although the vorticity correlation may not always yield velocity fields that are the most similar, the velocity fields associated with these best-correlated pairs consistently demonstrate high similarity; the best-correlated pairs for $\theta_f = 0°$ at 0.6D consistently show the highest center bypass flow among the fields at their respective locations. Conversely, the best-correlated pairs for $\theta_f = 90°$ at

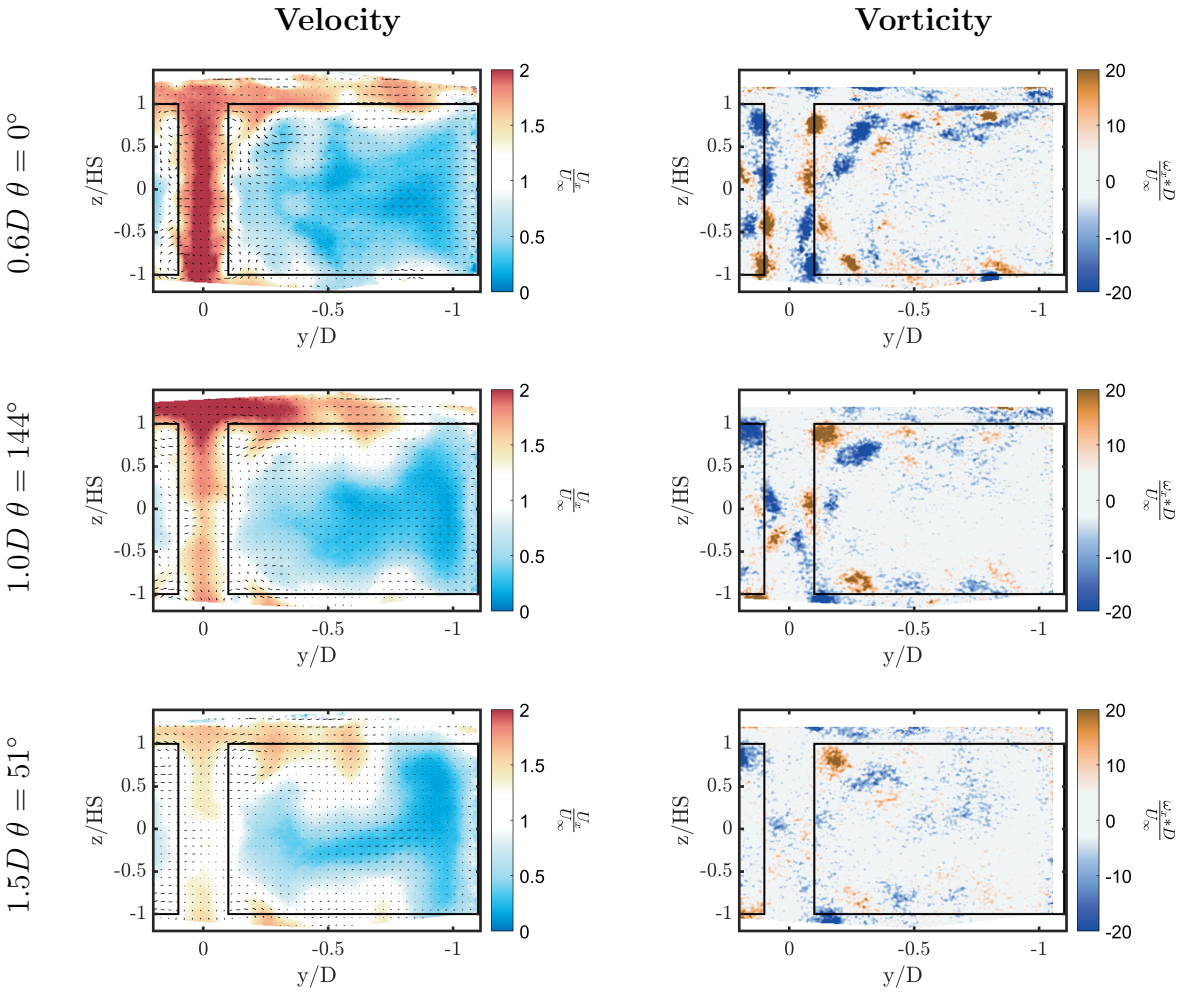

Figure 4.8: Best 0.6D, 1.0D, and 1.5D correlated pairs at $\theta = 0°$, $\beta = 55\%$

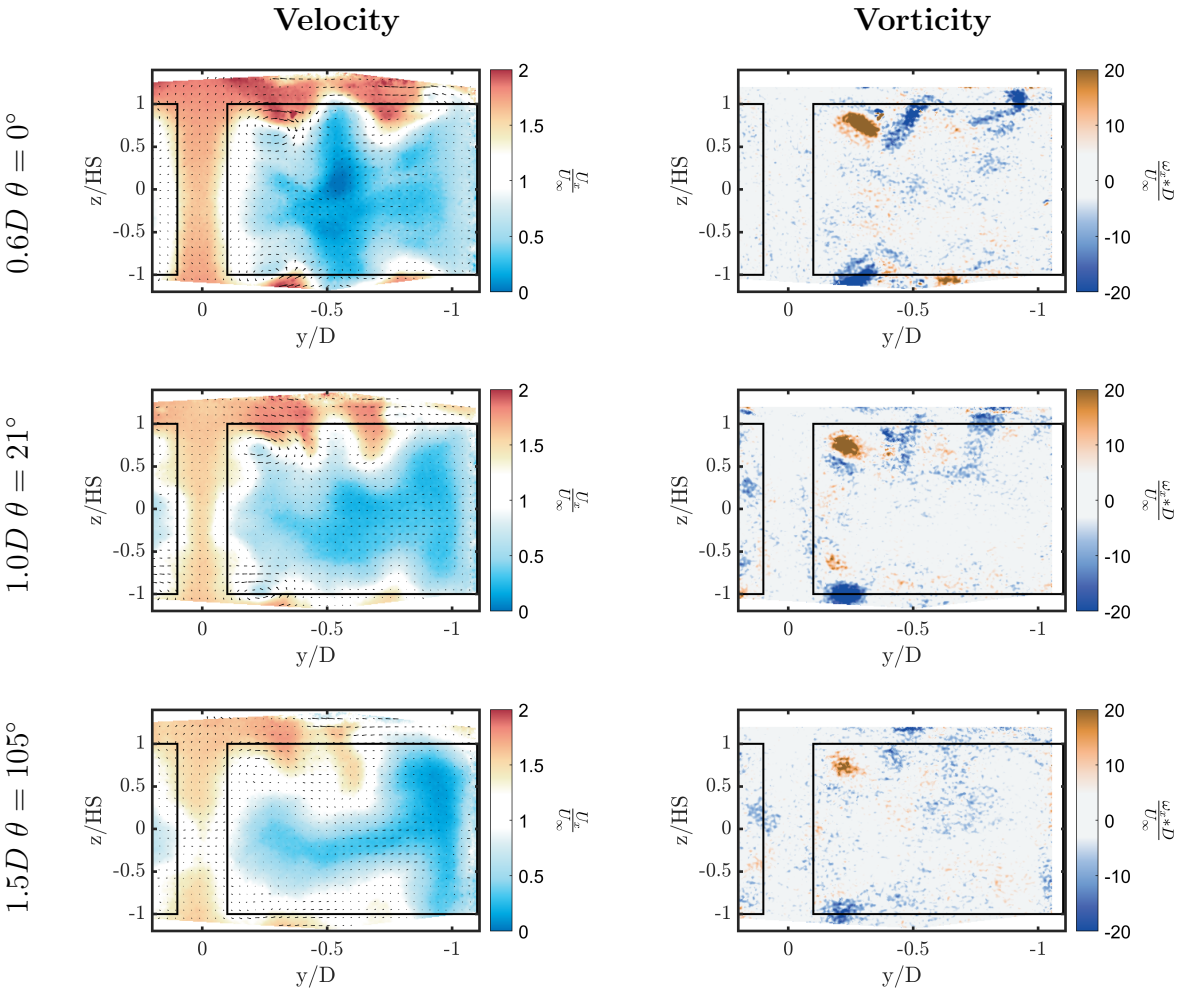

Figure 4.9: Best 0.6D, 1.0D, and 1.5D correlated pairs at $\theta = 90°$, $\beta = 55\%$

0.6D consistently exhibit the lowest center bypass flow. These results support the validity of characterizing the instantaneous flow field through its vorticity

In general, vorticity values decrease and vortices become less concentrated in downstream positions, which is typical due to dissipation. At 1.5D, the tip vortices maintain their presence and show minimal upward movement from the induction effects in the $\beta = 55\%$ case, although their spacing is noticeably increased. The two blue vortices adjacent to the red tip vortex merge into a single vortex as they move downstream. Additionally, the group of scattered vortices at the top of the wake region becomes barely noticeable by 1.5D.

The cross pattern in the flow is also barely recognizable at 1.5D. These vortices appear to increase local momentum mixing significantly as the flow region dominated by this cross pattern in the center bypass recovers to the free stream velocity much quicker than the surrounding center bypass flow. Moreover, the increased mixing might cause the viscous effects to diffuse vorticity in these smaller cross-pattern vortices more than in the larger ones such as the tip vertices. Each vortex within the cross pattern seems to induce velocity on the others, with slightly larger vortices inducing higher velocities than smaller ones. This interaction may explain why vortices move closer to the center as they travel downstream.

In the center bypass, the high-velocity fluid moves to the top and bottom sections. The in-plane velocity field suggests that this movement is propelled by the high induction from the tip vortices. Observation suggests that the large tip vortices do not mix the momentum as well as the ones in the cross pattern but mostly advect flow from the center bypass into the top and bottom bypass.

The wake exhibits higher velocity on the bypass side compared to the wall side. As the wake progresses downstream, the corners on the bypass side shrink noticeably. Concurrently, the downwash in the top bypass and the upwash in the bottom bypass intensify significantly later downstream, causing the top and bottom surfaces of the wake to drastically recess. Meanwhile, the height of the wake on the wall side remains constant, and the in-plane velocity vectors indicate that flows are moving into this region, suggesting that its pressure is lower than in other areas.

At $\theta = 90°$, the impact of the center shaft becomes more apparent. As the field is convected downstream, the center shaft wake's effect on the flow gradually diminishes, allowing the separated downward-moving flow to begin merging. This merging significantly increases the entrainment from both the top and bottom bypass into the wake, contributing to a more pronounced change in the wake shape between 1.0D and 1.5D compared to the upstream segment.

Fig4.10 and 4.11 display the best-correlated pairs determined by the correlation method introduced at $\theta = 0°$ and $90°$ respectively when $\beta = 45\%$. It was later discovered that the turbines θ were not synchronized by mistake when the 1.0D plane data were recorded during the experiment. As a result, the flow symmetry behind the two turbines was broken, and the center bypass exhibited strong lateral movement as shown in these figures for fields at 1.0D. The vorticity field at $\theta = 0°$ shows a significant difference between the two turbines. The uneven forces exerted by the two turbines on the flow distort the vortex structures. Details about how this affects the correlation will be discussed in the next section.

The fluid structures at 1.5D are very similar to the $\beta = 55\%$ case, the tip vortices have higher vertical displacement likely due to the free surface being further away. With the tip vortices being further away from the wake, the vortex entrainment has less effect on its shape and the size of the wake does not shrink as much as $\beta = 55\%$ case. Vortices and downwash from the free surface are weaker in lower β, which may explain why the wake flow shape does not change as much moving downstream.

Best-correlated pairs for $\beta = 35\%$ are shown in Fig4.10 and 4.11. The flow shows a similar evolution as the higher β cases. The tip vortices travel further as the free surface is more distant. The cross pattern shows a stronger concentration at 1.0D compared to 0.6D. This may be attributed to the three-dimensional interactions between the vortices that result in a more significant streamwise component momentarily at 1.0D. Although the flow in the bypass recovers to U_∞ more quickly, the wake size at 1.5D is larger than that observed with $\beta = 55\%$, suggesting a longer wake recovery distance at lower β.

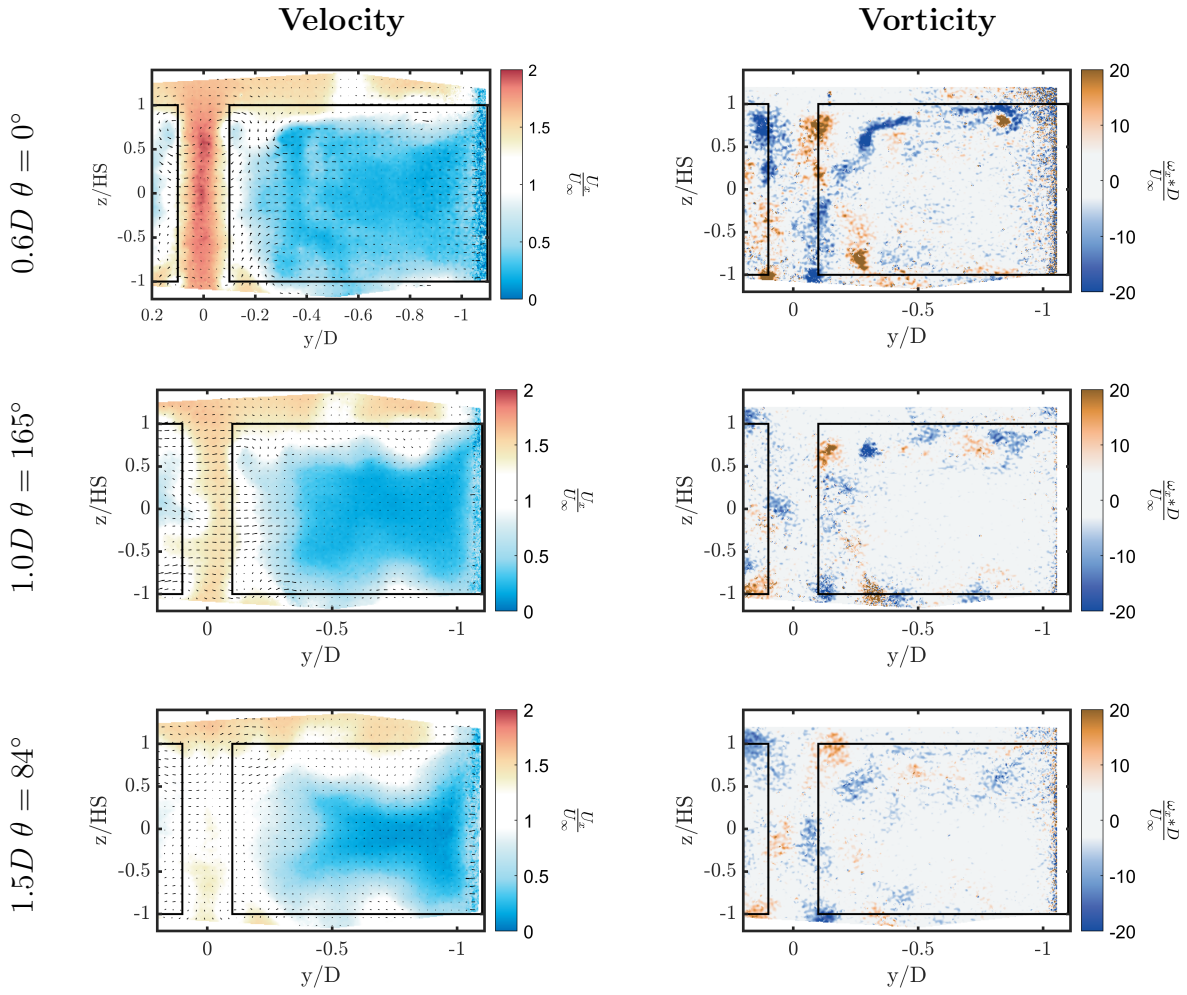

Figure 4.10: Best 0.6D, 1.0D, and 1.5D correlated pairs at $\theta = 0°$, $\beta = 45\%$

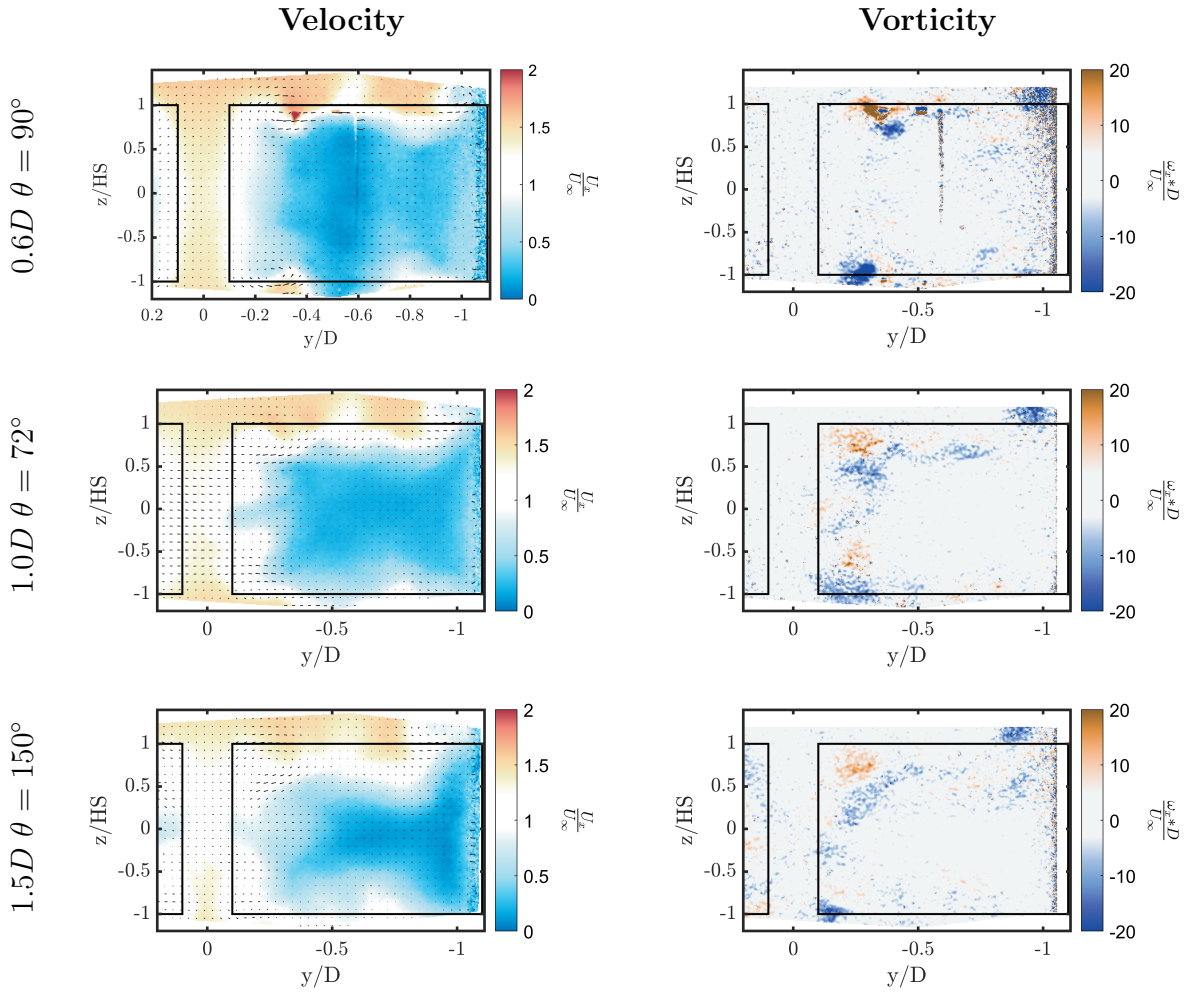

Figure 4.11: Best 0.6D, 1.0D, and 1.5D correlated pairs at $\theta = 90°$, $\beta = 45\%$

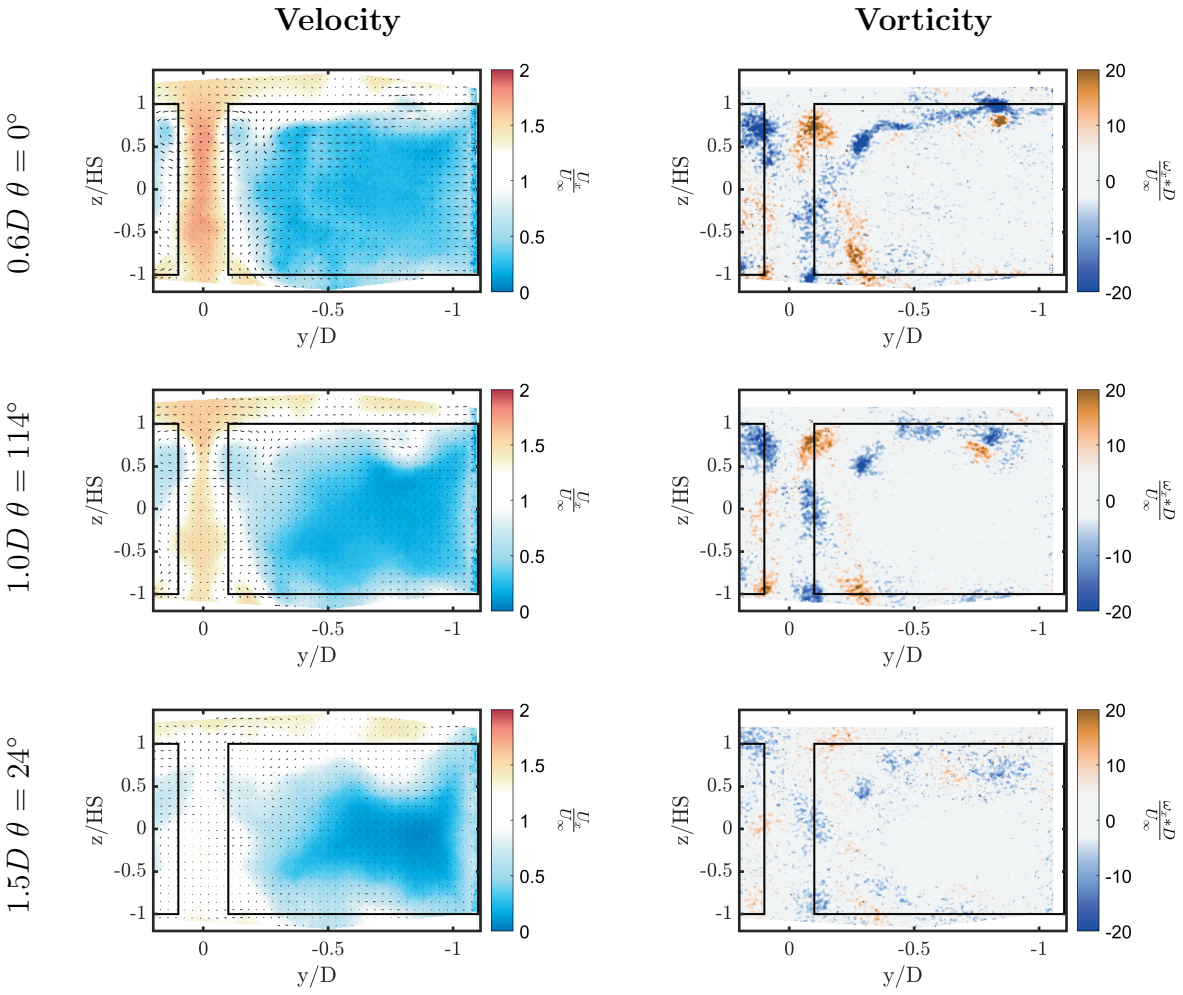

Figure 4.12: Best 0.6D, 1.0D, and 1.5D correlated pairs at $\theta = 0°$, $\beta = 35\%$

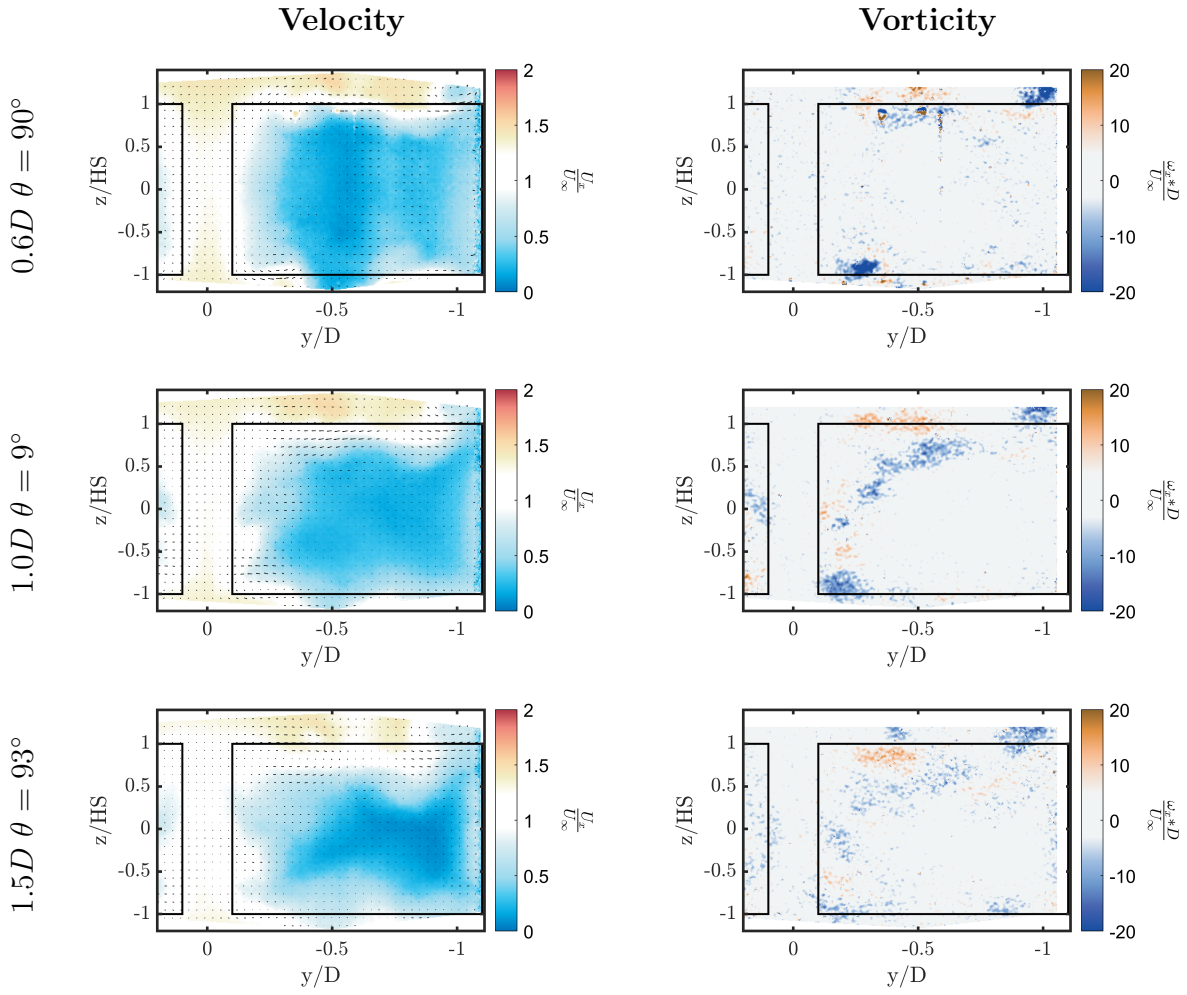

Figure 4.13: Best 0.6D, 1.0D, and 1.5D correlated pairs at $\theta = 90°$, $\beta = 35\%$

4.4 *Study of the impact of confinement and position on convective velocities*

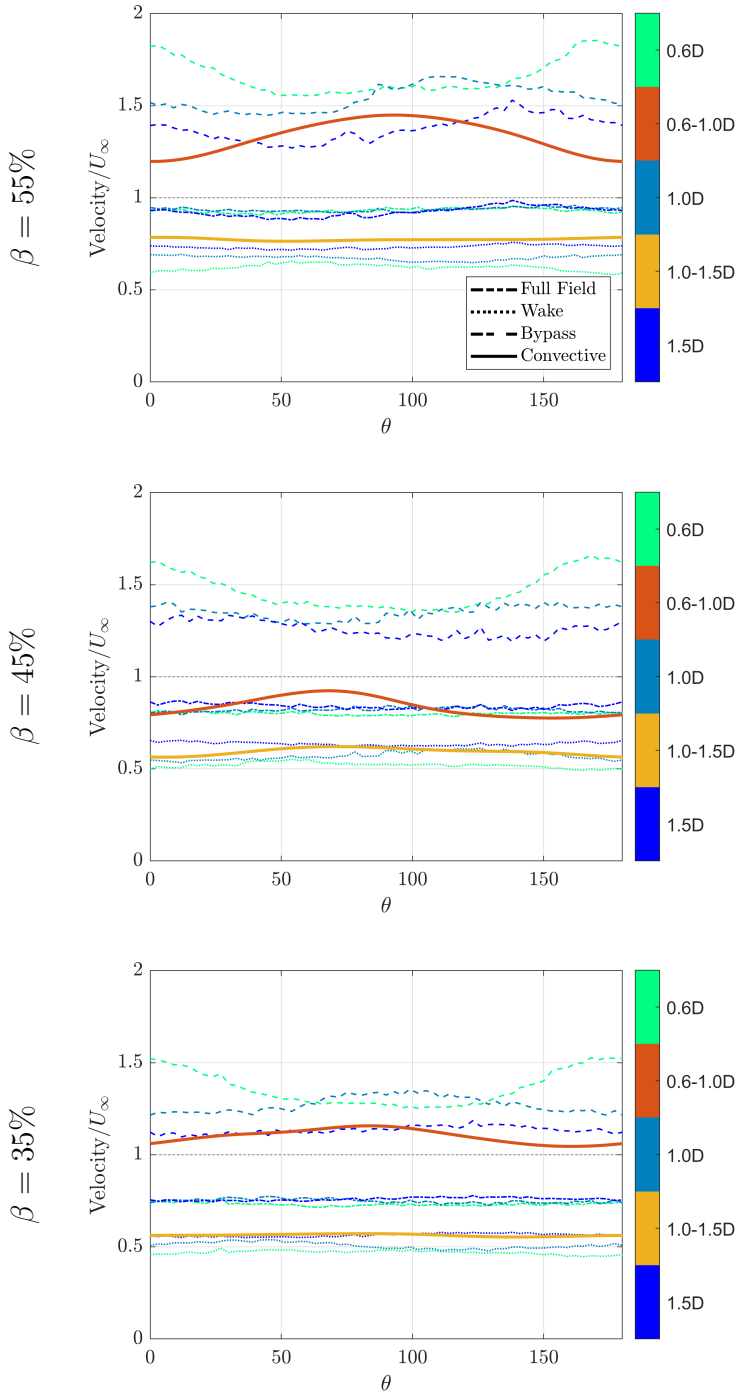

Figure 4.14: Average and convective speed comparison. The angle θ corresponds to the phase position of the blades at the time of acquisition of the most upstream plane.

The average streamwise velocity is compared with calculated best estimates of the convective velocity for the full field, wake, and bypass region in Fig 4.14. Convective velocities are calculated using the method described in Section 4.2, utilizing the phase difference of best correlation of the streamwise vorticity field between two streamwise locations. The "full field" region encompasses the entire domain where PIV data are available. The convective speed, U_c, curves reflect the U_c corresponding to θ the upstream field in the correlated planes, and the averaged field curves represent the instantaneous averaged velocity within a specified region for the specified turbine θ. It is observed that the bypass average is significantly higher than the wake's, with the full field average falling in between. The convective speed from 0.6D to 1.0D lies between the bypass and the full field average at 0.6D, and from 1.0D to 1.5D, it falls between the full field and wake average.

The normalized velocities in all regions increase with higher β values. For all β, the bypass exhibits the highest average velocity at 0.6D, which decreases as the flow is convected downstream. Conversely, the wake shows the lowest average velocity at 0.6D, which then increases at further downstream positions. This trend is expected due to the momentum transfer between the two regions.

The most prominent vortices are formed near the boundary between the bypass and wake regions. Across all β values, the vortex structures initially exhibit speeds higher than the wake average but lower than the bypass average at $\theta = 0°$. Their highest speed aligns with the trough in the bypass flow, suggesting that the vortices entrain part of the streamwise momentum to accelerate themselves shortly after passing the turbine.

For all β except for $\beta = 45\%$ case that is affected by the mistake in the experiment, the 0.6D to 1.0D correlation yields the best pair $\Delta\theta$ in the range of 100° to 150°, indicating that the field takes less than half a cycle ($< 180°$) to reach the next data plane. For 1.0D to 1.5D, an appropriate range was found to be 200° to 350°, meaning the field takes more than half a cycle to advance to the next plane, suggesting that the convective speed in this later interval is much slower than in the previous one.

Figure 4.15 presents the convective speeds for different blockages and streamwise posi-

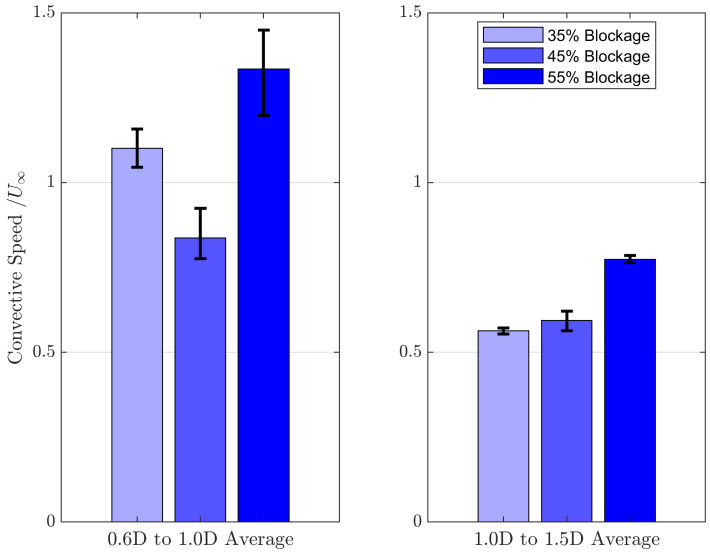

Figure 4.15: Convective Speed Comparison. The $\beta = 45\%$ case appears to be much lower than expected in the forward section.

tions averaged across all θ, with error bars representing the variation observed for this mean. Consistent with earlier observations, the convective speed increases with higher β and decreases with distance downstream, with one exception. The 0.6D to 1.0D convective velocity is much lower for the 45% case compared to the other blockages and is even lower than U_∞. This led to the discovery that there was a non-zero phase offset between the turbine for 1D plans data, hence the $\beta = 45\%$ will not be considered moving onward.

4.5 Volumetric Reconstruction

4.5.1 In-plane Vortex Structures

The convective velocities explored in the previous section were then utilized to create three-dimensional estimates of the flow field evolution following the method outlined in Section 4.2. Fig 4.16 shows isosurfaces of the streamwise component of vorticity for the case with

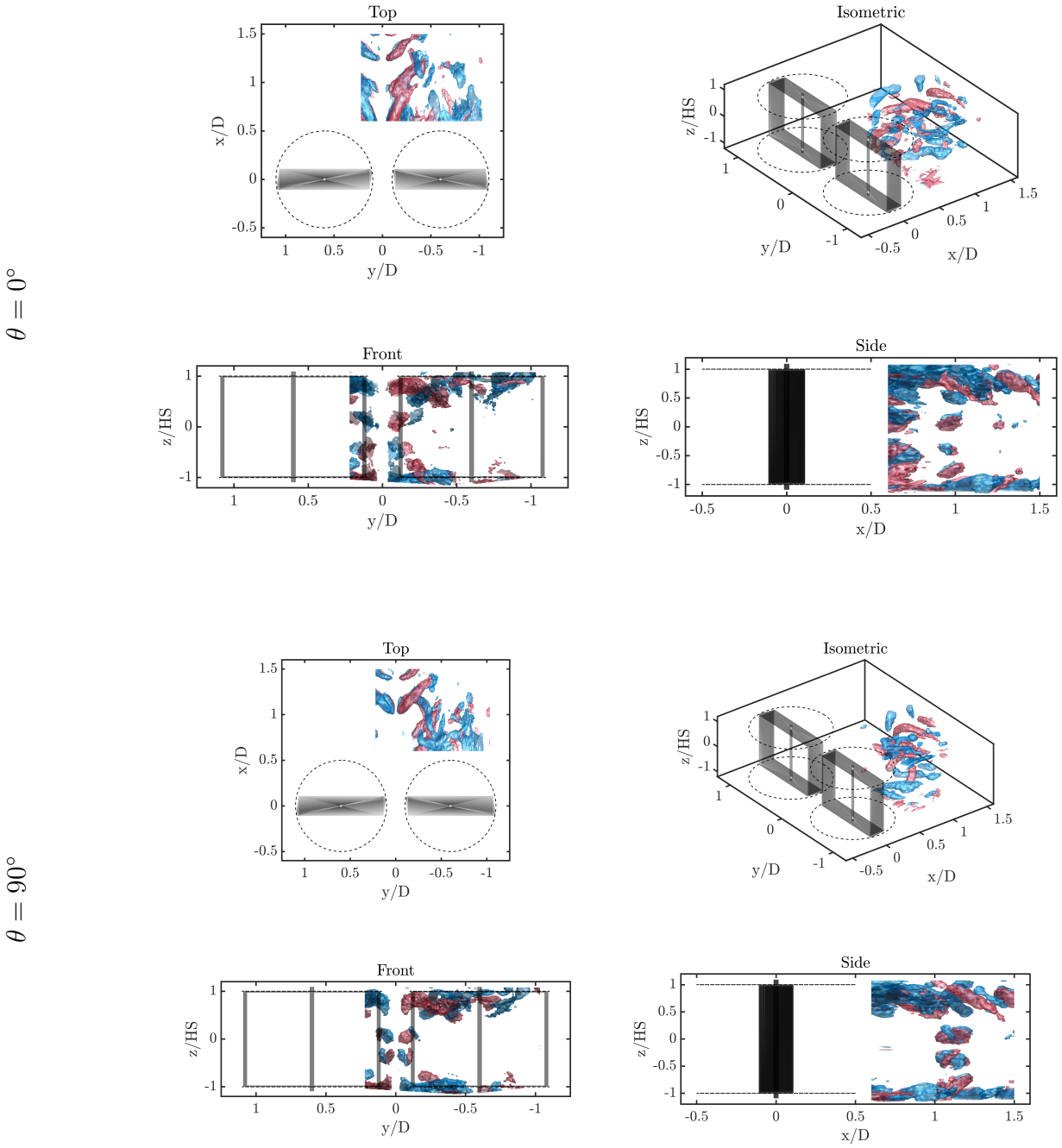

Figure 4.16: Volumetric Isosurface for $\omega_x = \pm 20$ normalized by $\frac{D}{U_\infty}$ at $\theta = 0$ & 90°, $\beta = 55\%$. Red surfaces denote vortex in the positive x direction, and blue surfaces are for the negative x direction.

$\beta = 55\%$ blockage. To facilitate direct comparison across all β cases, the threshold for the isosurfaces is uniformly maintained at $\pm 8\frac{U_\infty}{D}$ in both scenarios. This specific surface value has been determined to be the most effective for highlighting the vortex structures across all β levels. Figures with different isosurface values were investigated during the analysis to draw conclusions, but they are not presented here to keep the paper concise. The free surface heavily influences a section of the top bypass region and has been cropped to provide a cleaner view. The cropped region is a rectangle with a height around $0.1D$. The red isosurfaces highlight the vortex pointing in the streamwise direction according to the right-hand rule and the blue ones in the opposite direction. The estimation of other components of the vorticity has a high sensitivity to the estimation of convective velocity so ω_x is selected for initial examination as it is the most accurate component because it is calculated using displacement and blending of the original recorded velocity fields.

Coherent vortex structures are observed in the reconstructed flow field. The tip vortices are the most concentrated and the strongest structure in the flow. They are shed every half a cycle of the turbine rotation. The cross pattern also shows a strong presence at the mid-span of the turbine and is generated at $\theta = 0^\circ$ as shown in Fig 4.16. Above the wake region, the $\theta = 90^\circ$ case exhibits a higher concentration of blue vortices than the $\theta = 0^\circ$ case. Additionally, the top bypass region features complicated interactions between these blue vortices and the tip vortices. These observations are all consistent with the planar field features mentioned earlier.

From 1.0D to 1.5D, the fluid structures are well synchronized as the convective speeds are slower, causing the vortices to remain coherent. This coherence suggests that the convective velocity calculated from the correlation is a decent estimate of the true convective speed in this later interval. However, from 0.6D to 1.0D there is a presence of two tip vortices at $\theta = 0^\circ$ which remain highly similar in shape. At $\theta = 90^\circ$, the tip vortex becomes discontinuous in this forward section. These observations suggest that the tip vortices captured by the blended flow field estimate (0.6D downstream and 1.0D upstream) are not synchronized.

As discussed in Section 5.5 regarding the calculated convective speeds, the frames at

0.6D take less than half a cycle to reach 1.0D. Consequently, only a single coherent tip vortex structure should be present within this interval since a tip vortex is generated every half cycle. This desynchronization is likely due to an underestimation of the convective speed in this interval. When the convective speed is underestimated, the downstream extrusion from 0.6D does not travel as far downstream as quickly as it should, and similarly for the upstream extrusion from 1.0D. Consequently, two copies of the same structure appear. To address the synchronization issues observed between 0.6D and 1.0D, future studies should consider adding additional PIV data planes within this interval.

The same issue also impacts the visualization of the cross pattern at the bypass vertical center in the forward section of the blended volumetric flow (0.6-1.0D). Ideally, a perfect reconstruction should depict the cross pattern as a single continuous structure within this interval, consistent with earlier planar field observations showing it is generated every half cycle. While there are limitations to this reconstruction, the flow field analysis should still qualitatively capture the evolution of the vortex structures.

It is also important to note that in inviscous flow, every cross-section of the vortex filaments conserves the total circulation. When this filament is compressed, the cross-sectional area of the filament increases and causes the vorticity per unit area to decrease. This vortex compression may be misinterpreted as a decrease in the vortex circulation that characterizes its strength when plotting in isosurfaces. This limitation is an inevitable aspect of the visualization technique used in this work.

The vortex structures need to be identified before further accessing their effect on the bypass and wake evolution. The major vortex structures in the ω_x component are categorized as upwind blade tip vortices, downwind blade tip vortices, cross pattern vortices, and top shearing vortices. Each type will be individually assessed and presented in the following paragraphs. To enhance visibility and highlight the distinct characteristics of each vortex type, the y and z axes ranges for the figures depicting these structures will be adjusted accordingly.

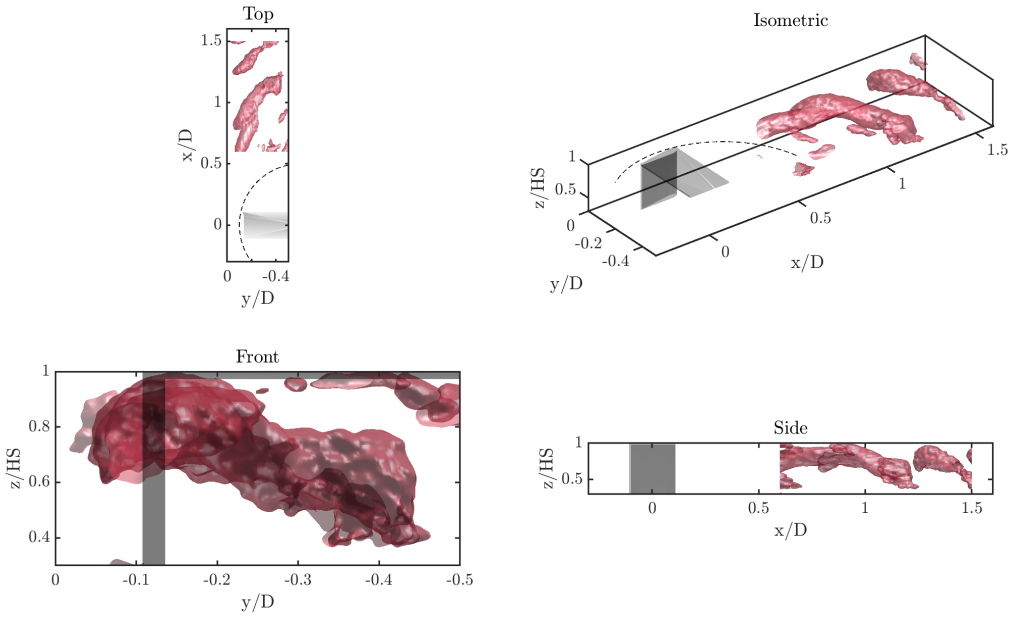

Figure 4.17: $\beta = 55\%$ $\theta = 0°$ downwind tip vortex structure and isosurface face value is set to $8\frac{U_\infty}{D}$

Fig 4.17 illustrates the tip vortex generated by the blade as it moves downstream from $\theta = 90 - 270°$. As the blade rotates downstream from $\theta = 180°$, the tip vortices it produces have a decreasing component in the streamwise direction. Consequently, the true extent of the tip vortex may be much longer than what is depicted in the extrusion, but this extent is not captured in the current visualization.

The lateral movement of the downwind blade tip vortex is primarily due to its attachment to the blade and the lateral induction caused by the turbine's rotation. As the tip vortex follows the blade into the top center of the wake, where fluids have significant components in the negative z-direction, it also descends with the fluid in this region.

The tip vortex extending from 0.6D to 1.0D appears much stronger and longer than the one behind it. This weakening of the downstream vortex is expected due to dissipation, but it may also indicate that the tip vortex's component in the x-direction diminishes as it is

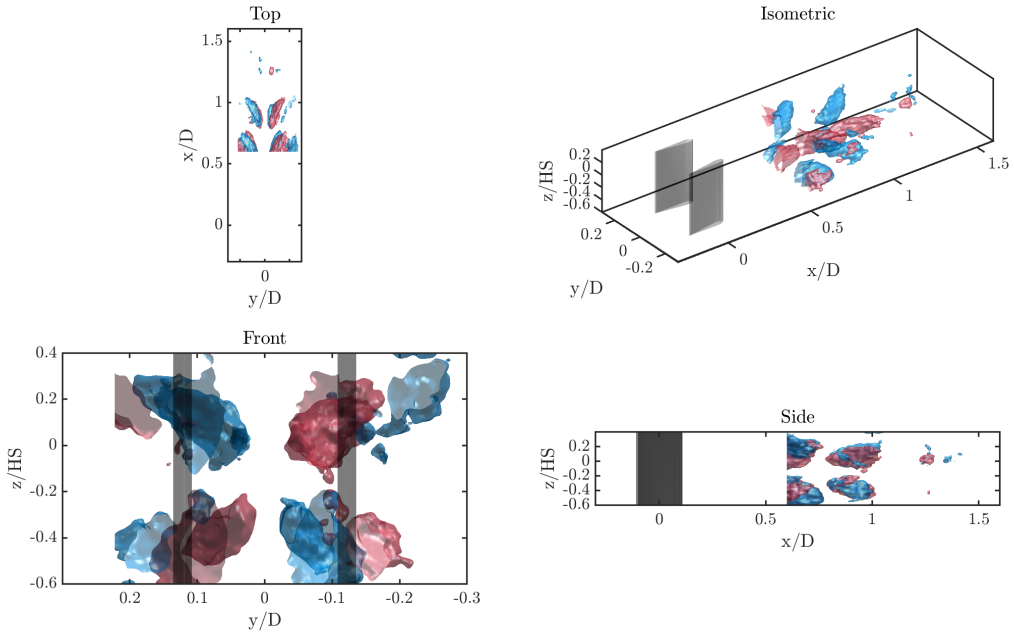

Figure 4.18: $\beta = 55\%$ $\theta = 0°$ cross pattern vortex structure and isosurface face value is set to $\pm 8\frac{U_\infty}{D}$

convected downstream. Additionally, as the vortex structure decelerates, the vortex string may be compressed, resulting in the distribution of circulation over a larger area and causing the vorticity concentration to decrease.

The center cross pattern displays intriguing, potentially highly three-dimensional interactions between opposite-magnitude vortices. Each leg of the cross pattern is likely to form a vortex ring, however the existence of rings is not confirmed by this figure. The cross pattern is not strong enough to be captured by the chosen isosurface at 1.5D and is not easily recognizable even with a much lower isosurface threshold. While convecting downstream, its size appears to decrease substantially as it moves in the streamwise direction. This observation supports the hypothesis that the structure significantly enhances local mixing, leading to the rapid dissipation of vortices due to high viscous stress.

As illustrated in Fig 4.19, the top of the wake section is dominated by negative streamwise

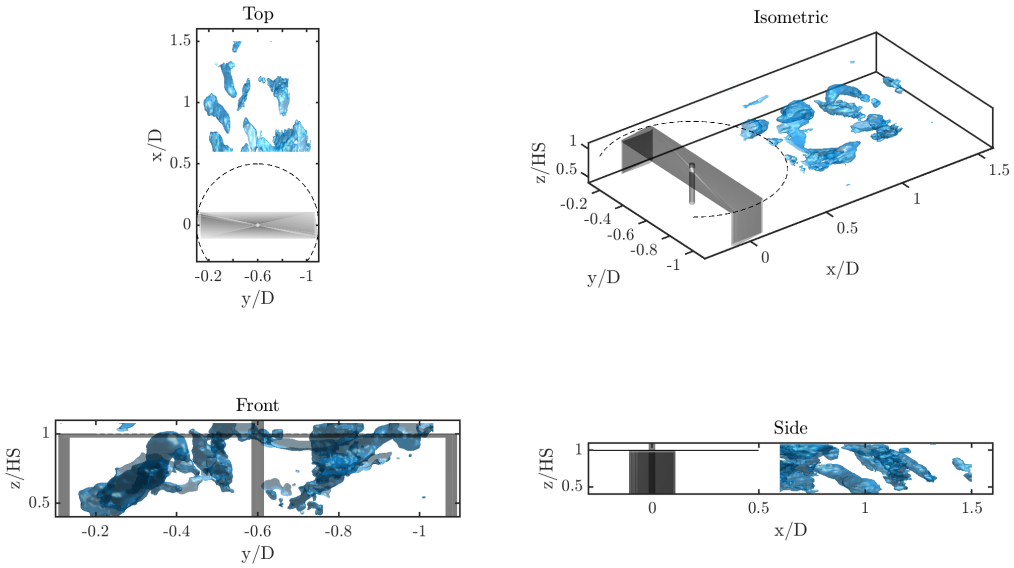

Figure 4.19: $\beta = 55\%$ $\theta = 0°$ shear vortices and isosurface face value is set to $-8\frac{U_\infty}{D}$

vortices. From the top view, the formation of several vortex strips is evident as protrusions emerge from the blue vortex region. These protrusions become discontinuous likely due to interaction with downstream blade tip vortices. The scattered negative vorticity does not extend much longer into the downstream direction unlike those protrusions. In the front view, these vortices exhibit the largest vertical displacement at the left top corner of the wake region and to the right of the center shaft, areas that coincide with the highest downwash observed in the planar views. From the side view, it appears that these vortices are entrained from the top bypass into the wake region, aligning with the observation that the wake top is predominantly influenced by downwash directly behind the turbine.

Based on these observations, the following mechanism is hypothesized for the formation of the negative ω_x vortices in this region. The long blue vortex closest to the wall side is likely the tip vortex from the upstream blade at $\theta = 0°$, which will be discussed in greater detail later in $\beta = 35\%$ case where it can be isolated more easily. The remainder of the

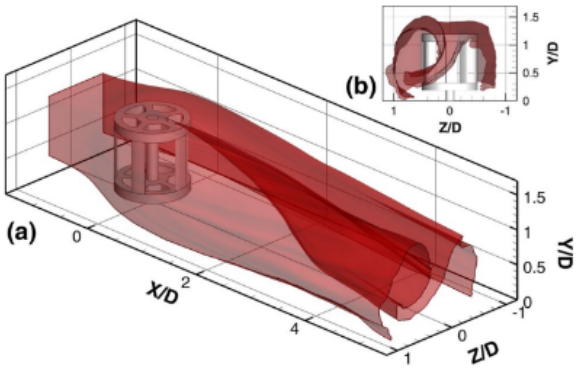

Figure 4.20: Time averaged stream surface that characterizes the wake evolution of CFT wake development from Ryan (2016)[2]

blue structure is likely generated by a shear layer resulting from transverse shearing in the flow. Opposite magnitude vortices can be observed beneath the wake regions, as shown in Fig 4.16. These vortices below the wakes are smaller, likely because they are closer to the floor boundary layer and are dampened. The presence of opposite shearing above and below the wake region indicates lateral shearing between the wake flow and the bypass flow, possibly influenced by the wing strut and turbine induction. While the turbine rotates, the flow above the top wing strut is faster than that below it. As the wing strut moves through the downstream half-cycle, it generates a shear layer, leading to the formation of negative streamwise vortices at the top. Since the flow at the top contains higher energy, the vortices above the strut dominate over the opposite shear layer vortices below it. This dominance results in the wake appearing more blue than red above the wake region.

The turbine induction may also contribute to the generation of these blue vortices. As the flow passes through the turbine core, it acquires a lateral velocity induced by the rotation of the turbine blades. This effect is evident in the averaged field, where the flow in the wake region is predominantly moving towards the side wall, away from the center bypass. In contrast, the flow that bypasses the turbine at the top does not immediately experience

this lateral acceleration. Consequently, the majority of the flow in the top bypass does not follow the same lateral direction as that in the wake. This difference in lateral speed causes transverse shearing between the wake and the top bypass, potentially contributing to the extensive blue region of vortices observed. Ryan (2016) [2] demonstrates a streamwise rolling of the wake boundary in time-averaged Magnetic Resonance Velocimetry (MRV) data, as shown in Fig 4.20, which may be attributed to the same phenomenon.

The shear layer, potentially arising from the wing strut and turbine induction, forms a vortex sheet composed of streamwise vortex filaments. This sheet is bisected by the flow diverting around the center shaft wake, with each half being compressed by the bypassing flow. This compression encourages the vortex filaments within each half to consolidate into larger, more distinct vortex strips, as depicted in Fig 4.19. From a top view, the lateral motion induced by the turbine's rotation advects these vortex strips to the right. En route, vortex filaments congregate along and attach to the left edge of the center shaft wake, thereby augmenting the growth of this vortex strip, while the right segment of the vortex sheet feeds into the upwind blade tip vortex.

Fig 4.21 display the same volumetric domain as Fig 4.19, highlighting the vortex structures at the top bypass region at $\beta = 35\%$. The isosurface value is kept the same as -8 $\frac{U_\infty}{D}$.As β decreases, the optimal λ also decreases, causing both the turbine's lateral induction and the wing strut shear layer to diminish. This reduction eliminates many shear vortices in the top bypass region, facilitating a better assessment of the large blue vortex near the wall.

In the top view of Fig 4.21, the two elongated vortices likely represent the tip vortices from the upstream moving ($\theta = 270 - 90°$) blade, each generated during different cycles of the turbine's rotation. These vortices exhibit the opposite sign to the downwind vortex highlighted in Fig 4.17. They also adopt an arc shape similar to that of the downwind blade tip vortex, a shape change that likely results from the change in the direction of the tip vortex as the blade rotates. Additionally, a video illustrating the field's progressive change with θ indicates that this vortex is generated every half cycle, mirroring the behavior of the downstream tip vortex." Furthermore, Ryan (2016) discusses a strong tip vortex pair in the

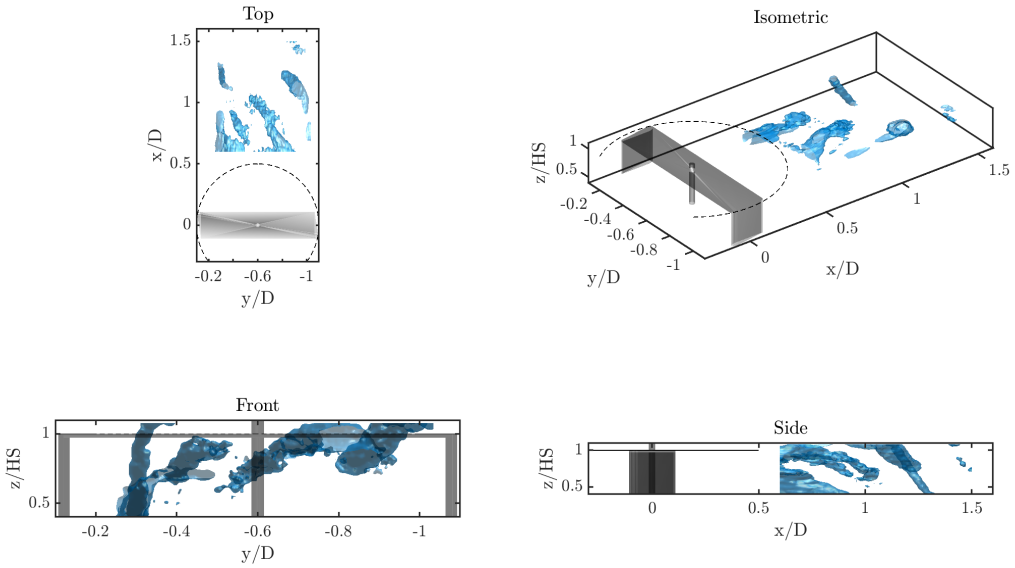

Figure 4.21: $\beta = 35\%$ $\theta = 0°$ upstream tip vortex and isosurface face value is set to $-8\frac{U_\infty}{D}$

upwind cycle and its significant effect on entrainment, suggesting that these upstream blade vortices should be detectable in our experimental setup.

The bottom tip vortex from the upstream blade is not observed in the reconstruction. This absence is likely due to its magnitude being reduced by the boundary layer of the floor, and it may deflect downward and move beyond the detectable region, rendering it invisible in the current visualization setup.

After all of the major streamwise vortex structures are identified, their changes with β can now be better assessed in Fig 4.22 that shows the streamwise vortex isosurfaces for $\beta = 35\%$. Comparisons will be made between this figure and Fig 4.16. In cases with lower β, smaller vortex structures are observed in the isosurface plots. This is likely due to inherently weaker vortex circulation in lower β scenarios, rather than a reduction in vorticity from compressed vortex tubes caused by streamwise velocity gradients, which are much lower in this case.

The disparity between the vortex structures in the two extrusions in the forward section

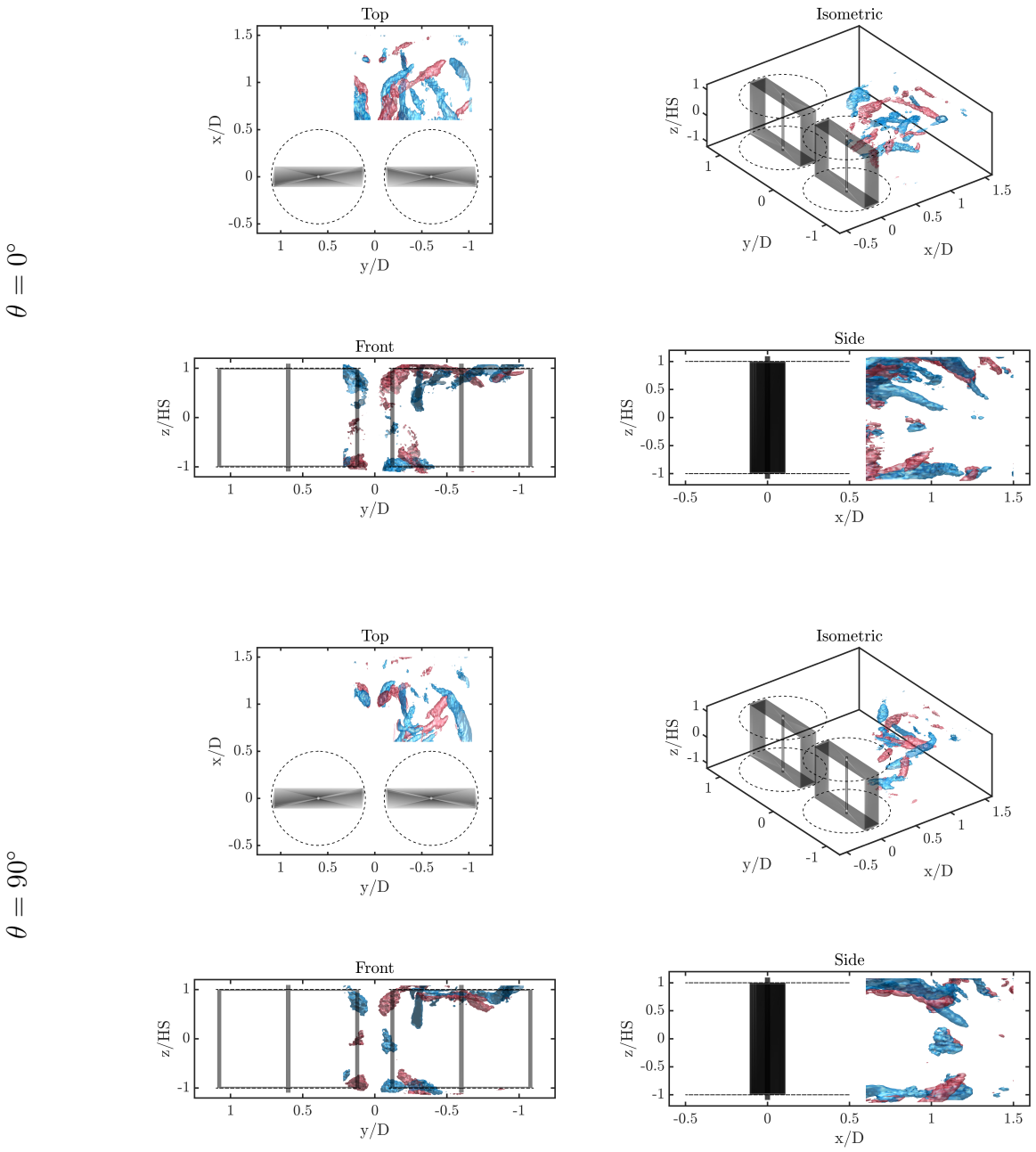

Figure 4.22: Volumetric Isosurface for $\omega_x = \pm 20$ normalized by $\frac{D}{U_\infty}$ at $\theta = 0$ & $90°$, $\beta = 35\%$. Red surfaces denote vortex in the positive x direction, and blue surfaces are for the negative x direction

(0.6 - 1.0D) is not as pronounced as in the $\beta = 55\%$ case, and the tip vortices are coherently connected. This lower blockage results in a much lower bypass velocity, a weaker vortex structure, and a smaller relative velocity between the regions. Consequently, the vortex should experience a smaller change in its convective velocity when mixing momentum between the regions. As a result, the linear interpolation of the convective velocity yields a smaller error, making the reconstruction more accurate to the actual flow. The high consistency and smooth transition as vortex structures shift through the extrusions suggest that the reconstruction method utilized here provides a good first-order estimation of the true volumetric flow.

Downstream tip vortices are notably smaller and become discontinuous where they intersect with shear vortex strips. These vortices are thinner in the forward section (0.6 - 1.0D), suggesting a smaller vortex cross-sectional area that renders them more vulnerable to viscous dissipation. In the aft section (1.0 - 1.5D), these vortices experience a much greater reduction in size in the lower β case. The trajectory of these tip vortices in both cases remains similar in that they both exhibit cycloidal shapes that also curve downward behind the turbine wake. This pattern may also affect the upstream tip vortices when β is different. However, it is blended into the group of top shear vortices in $\beta = 55\%$ and cannot be isolated to make a definitive conclusion.

At $\beta = 35\%$ $\theta = 0°$, the cross pattern vortex is much weaker as shown in the front and side view. Nevertheless, at $\theta = 90°$, the cross pattern behind the 1.0D plane appears as two opposite vortices instead of eight previously at $\theta = 0°$, also showing higher volume and concentration. This increased concentration downstream may be due to three-dimensional vortex interactions that consolidate scattered vortices into a larger vortex with a more significant streamwise component.

As mentioned before, the top shear vortices are weaker and more scattered. Looking at the side view, these vortices exhibit similar inclinations due to the downward entrainment flow into the wake region.

4.5.2 Out-of-plane Vortex Structures

The volumetric reconstruction enables the calculation and exploration of ω_y, ω_z, and the magnitude of the three-dimensional vorticity vector, $|\omega|$, as depicted in Fig 4.23. Setting the isosurface to a higher value is necessary for a cleaner visual representation; otherwise, the vorticity structures in all three components would be superimposed together, making it impossible to distinguish individual vortex structures.

In both β cases, the magnitude of vorticity closely resembles ω_x, as shown in Fig 4.16 and 4.22. This similarity likely arises because the flow field estimates are predominantly extended in the x-direction, allowing vorticity in this direction to be detected more easily. This indicates a potential bias in the reconstruction towards highlighting streamwise vortices, not necessarily indicating that the flow is predominantly dominated by these vortices.

Helmholtz's theorems state that vortex lines tend to form loops. However, due to the bias towards the x component and limitations of the reconstruction mentioned earlier, caused by errors in convective velocity and the assumption that all vortices are convected at the same speed, a resolution high enough to capture such intricate structures cannot be achieved in this volumetric reconstruction.

Furthermore, the $|\omega|$ indicates that all vortices tend to undergo significant shrinkage in cross-sectional area as they are convected downstream. This suggests that viscous effects may significantly dissipate the circulation within the vortex lines, making the detection of closed loops even more challenging.

Fig 4.24 presents the isosurfaces with value set to $\pm 8\frac{U_\infty}{D}$ $\theta = 0°$ for $\beta = 55\%$ & 35%. Red vorticity points in the positive y direction. The velocity differential required to calculate vorticity in the y and z directions is highly sensitive to errors in convective velocity. Additionally, the evolution of the vortex in these two directions is not well captured, leading to significant uncertainty regarding the streamwise location and strength of these vortices. Therefore, this reconstruction can only suggest the presence of some vortex structures in these respective directions, without definitive conclusions about their precise characteristics

$\beta = 55\%$

$\beta = 35\%$

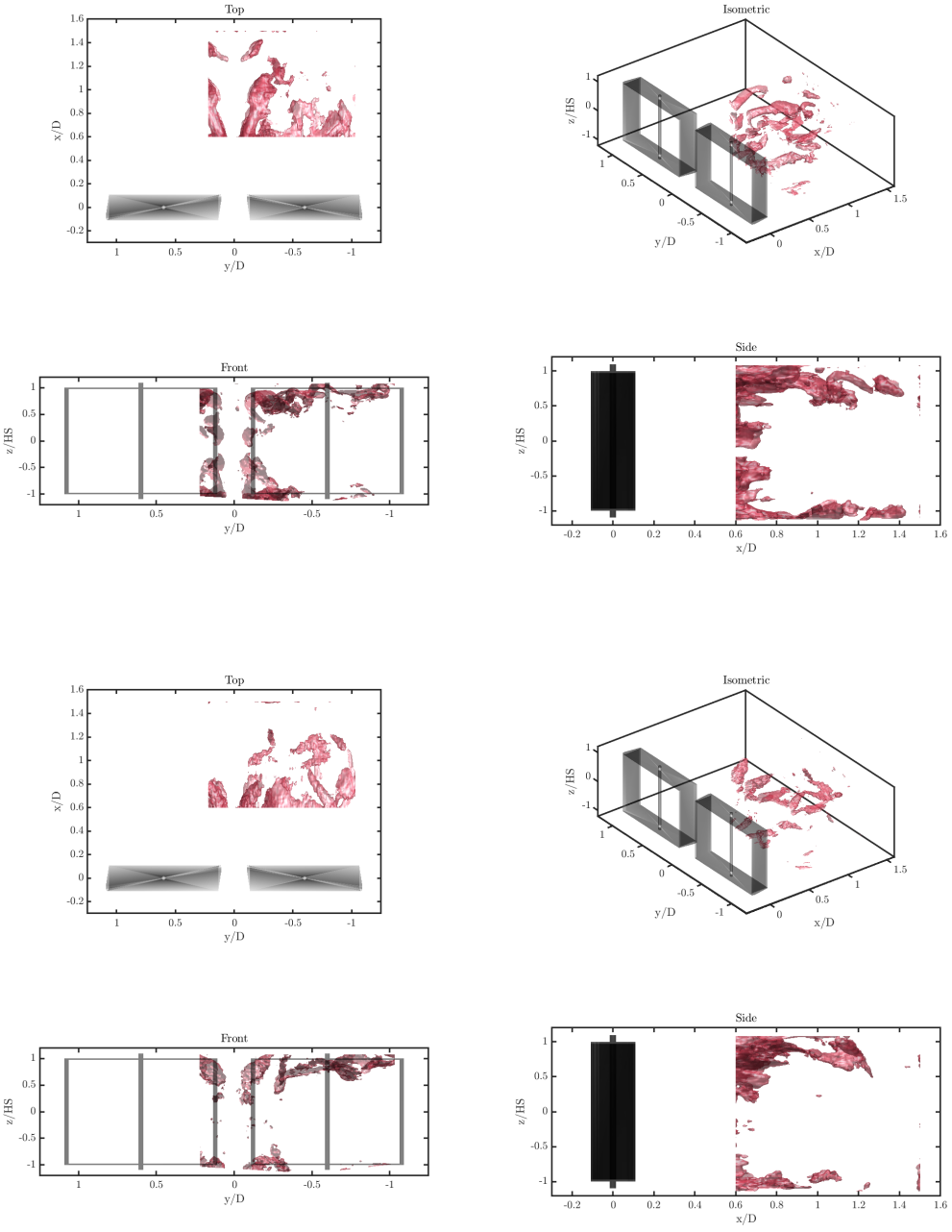

Figure 4.23: $\theta = 0°$ $|\omega|$ isosurface face value is set to 12 $\frac{U_\infty}{D}$ for $\beta = 55\%$ & 35%

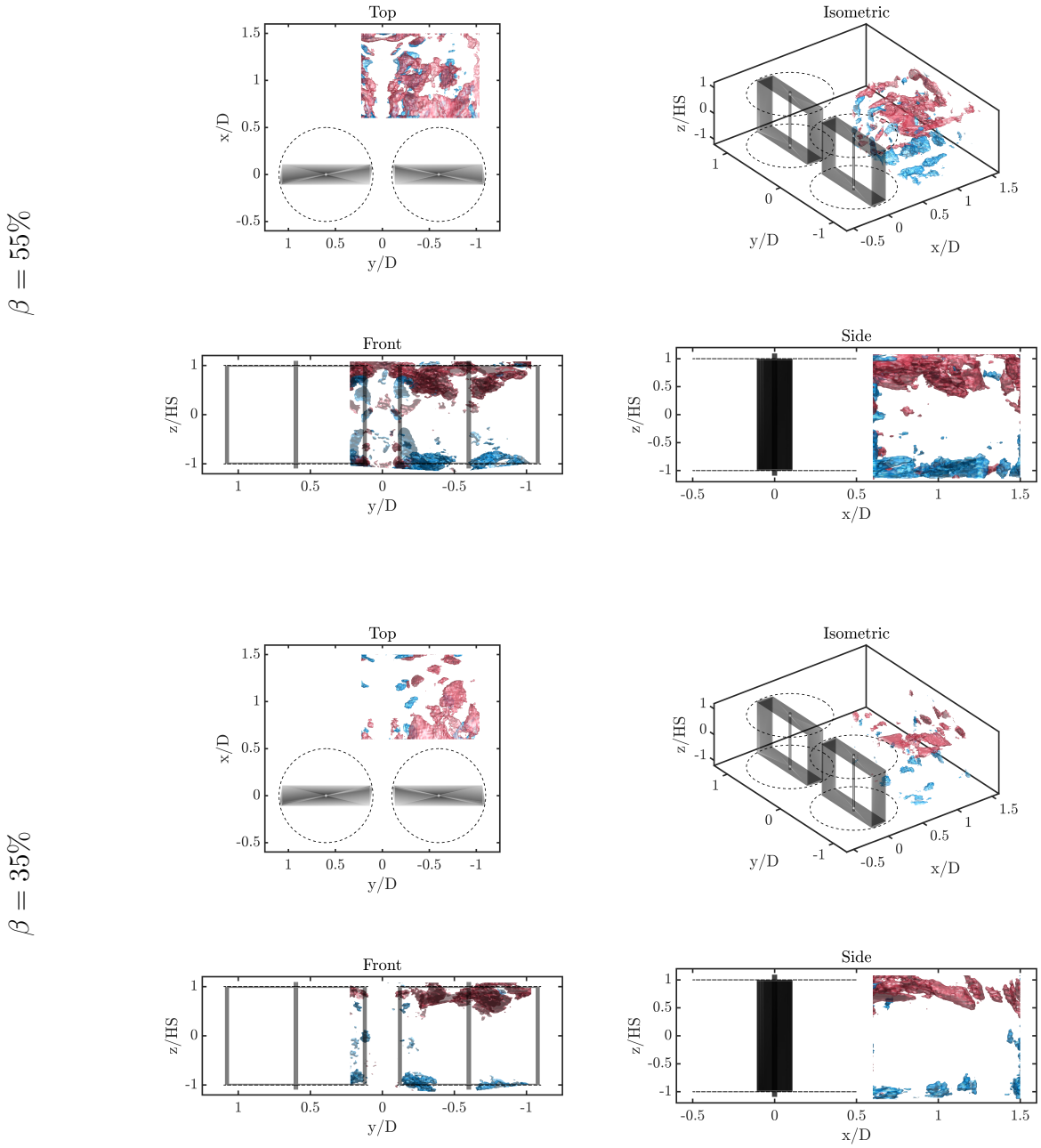

Figure 4.24: $\theta = 0°$ ω_y isosurface face value is set to $\pm 8\frac{U_\infty}{D}$ for $\beta = 55\%$ & 35%

or dynamics.

The top and bottom bypass move faster than the wake flow, leading to the development of opposite shear layer vortices at both the top and bottom of the wake for both β cases. This observation also shows that the top-shear vortices do not align strictly in the streamwise direction, as they exhibit a strong component in the y-direction as well. Meanwhile, The tip vortices may also exhibit strong components in the y-direction as their location aligns well with the region of high ω_y.

In both β cases a similar pattern is observed. ω_y is absent in the bypass region, indicating a lack of significant lateral vorticity. The cross-pattern vortices exhibit significantly smaller components in the y-direction compared to their streamwise components in x for $\beta = 55\%$. In $\beta = 35\%$, the presence of the cross pattern is barely recognizable.

The vorticity component ω_z for the volumetric flow field is presented in Fig 4.25 for the two β cases. The red vorticity points in the positive z direction. From the top view, the z-component of vorticity highlights strong shear layers between the center bypass and the wake for both β. The isosurfaces tend to change from continuous volume to discrete point concentrations within 1.0 - 1.5D, which can be best observed in the top view of $\beta = 55\%$, suggesting the formation of large eddies due to shear layer roll-up. Additionally, the vortices delineate the shearing between the center shaft wake and the rest of the top bypass flow in $\beta = 55\%$. When the isosurface value is set to a lower value, similar vortex structures are observed attached to the center shaft wake for $\beta = 35\%$, indicating that the wake from the center shaft significantly influences the flow dynamics in this region.

4.5.3 Velocity Components

Fig 4.26 presents the isosurfaces for velocity component U_x =75% & 125%U_∞ to investigate the evolution of the wake flow and bypass flow and the interaction between them. The red surface corresponds to the higher U_x value. The region encompassed by the blue surface can be defined to be the wake flow whereas the one enclosed by the red surface is the bypass flow. The space between these isosurfaces likely represents the shear region, indicating the

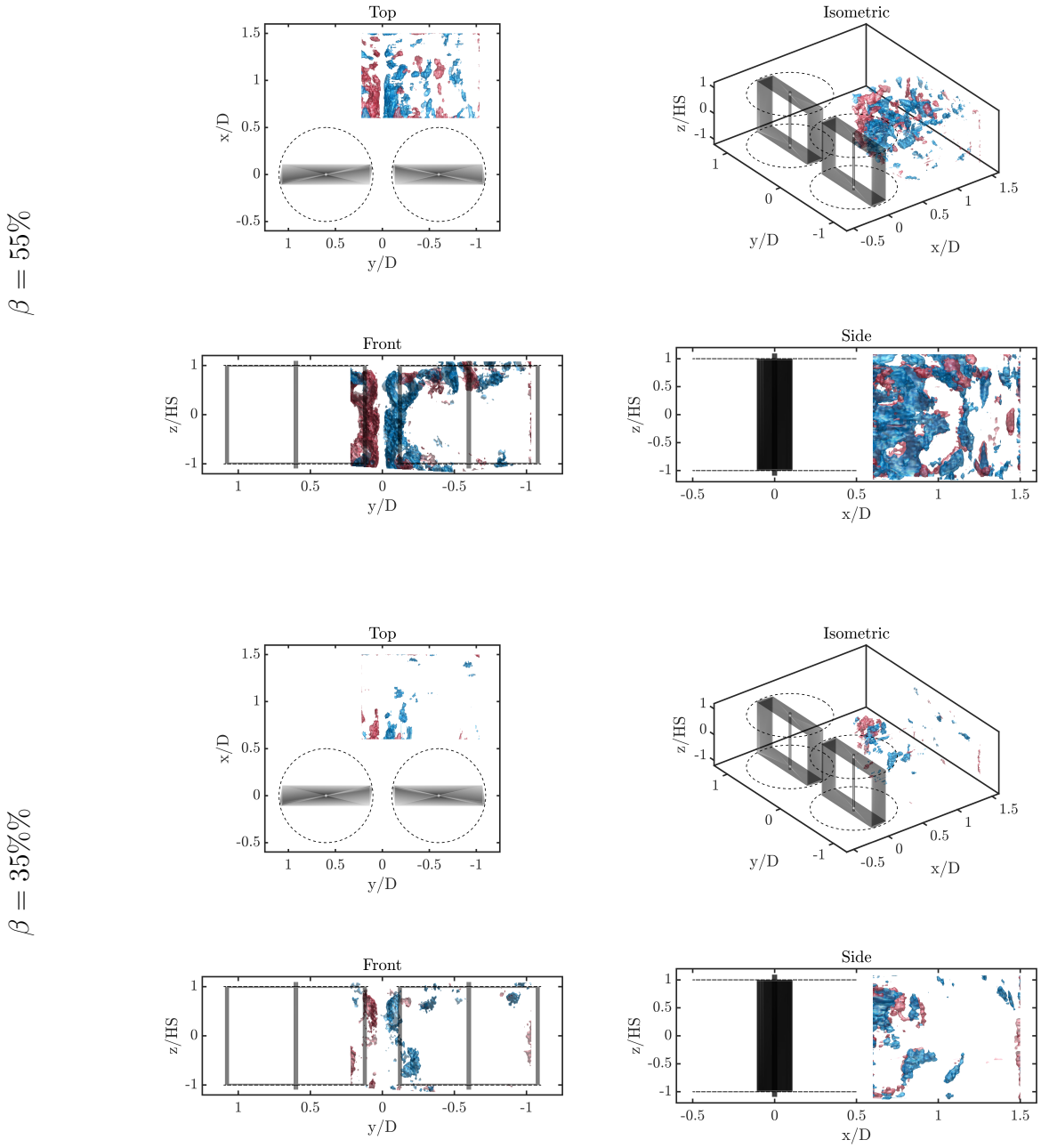

Figure 4.25: $\theta = 0°$ ω_z isosurface face value is set to $\pm 8\frac{U_\infty}{D}$ for $\beta = 55\%$ & 35%

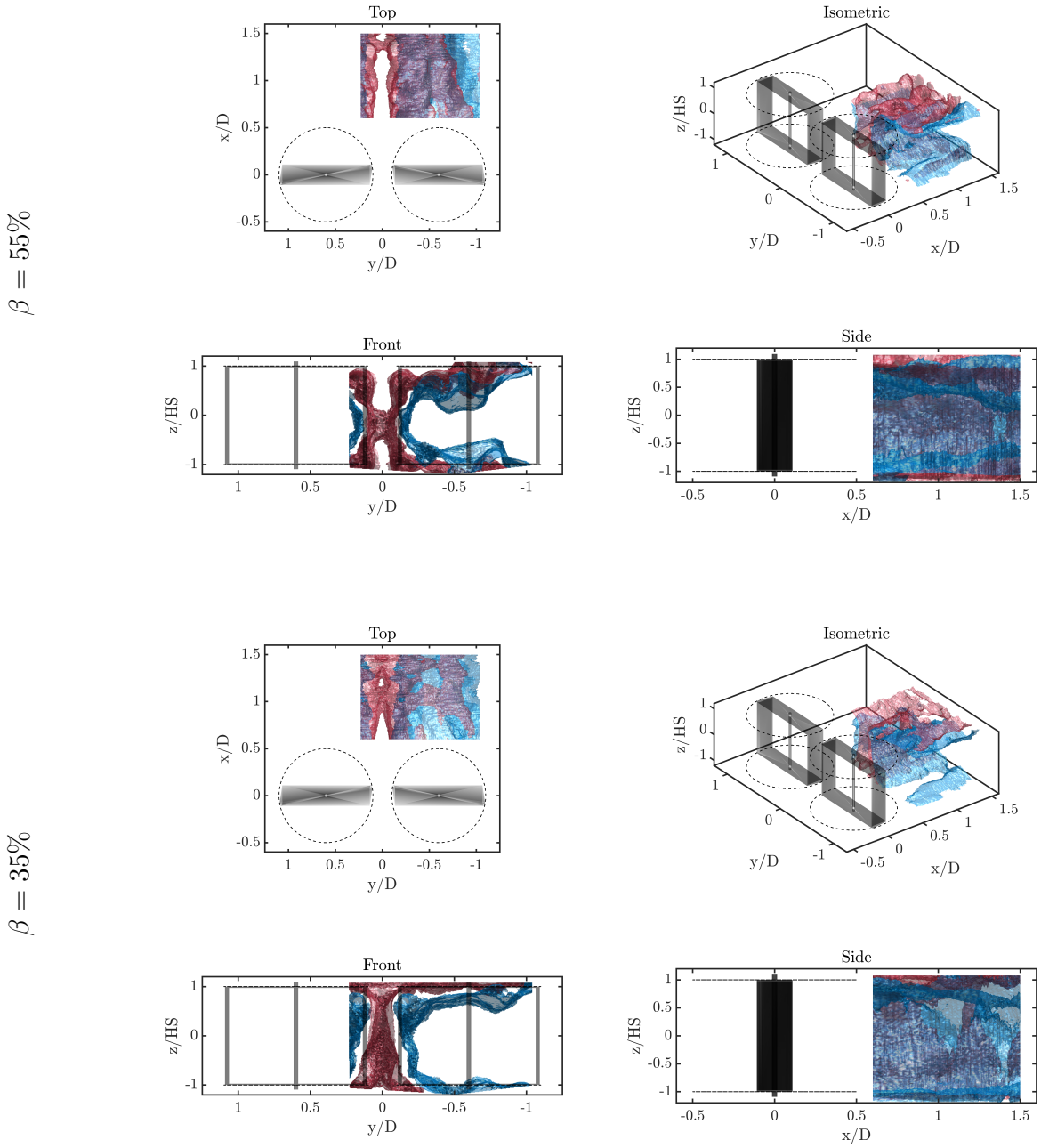

Figure 4.26: Blended volumetric isosurface for U_x= 75% & 125%U_∞, $\theta = 0°$, $\beta = 35\%$ and 55%

extent of momentum mixing that has occurred between the two regions.

Since the red surface encompasses the fastest bypass flow, the presence of the red surface means the flow passing outward through it must be decelerating. The red surface that splits the enclosed flow in the center bypass in the top and front view for both β means the high speed in the center bypass begins to decrease in magnitude at the mid-span. This reduction in speed is influenced by cross-pattern mixing, induction from tip vortices, and potentially a higher mid-span pressure that pushes fluids outward as described in previous sections. Despite this deceleration at the mid-span, the highest velocities remain at the top and bottom of the center bypass. From the front views, the top and bottom bypass show the slightest surface intersection in the bypass flow.

In the bypass, the functional differences between the tip vortices and the cross pattern become evident. The cross pattern generates shear stress that dissipates local momentum and slows down the fluid; however, the entrainment it causes is relatively low, as indicated by only minor lateral changes at the mid-span of the wake boundary. In contrast, the tip vortices facilitate the transport of higher velocity fluid from the center bypass to the top and bottom bypass regions, and subsequently into the wake. In the top views of both cases, the red surface moves further away from the side wall, which could be attributed to the convection due to the top shear vortices and the upwind tip vortices.

At $\beta = 55\%$, the bypass exhibits clear signs of rolling at the corners of the wake regions due to the influence of tip vortices, and the isosurfaces indicate much more intense mixing than $\beta = 35\%$. Since the cross pattern vortices are much stronger in the higher blockage case, the deceleration in the center bypass is more concentrated at the mid-span of the turbine. In $\beta = 35\%$, this local deceleration is reflected as a "waist" appearing in the red surface at the mid-span of the center bypass. The higher bypass velocity in the high-blockage scenario significantly reduces the cross-sectional area of the wake flow as can be seen in the front view, potentially reducing the wake flow recovering distance. However, the faster bypass also requires a longer distance to recover to U_∞.

The blue surfaces encompassing the wake flow from Fig 4.26 are isolated to better il-

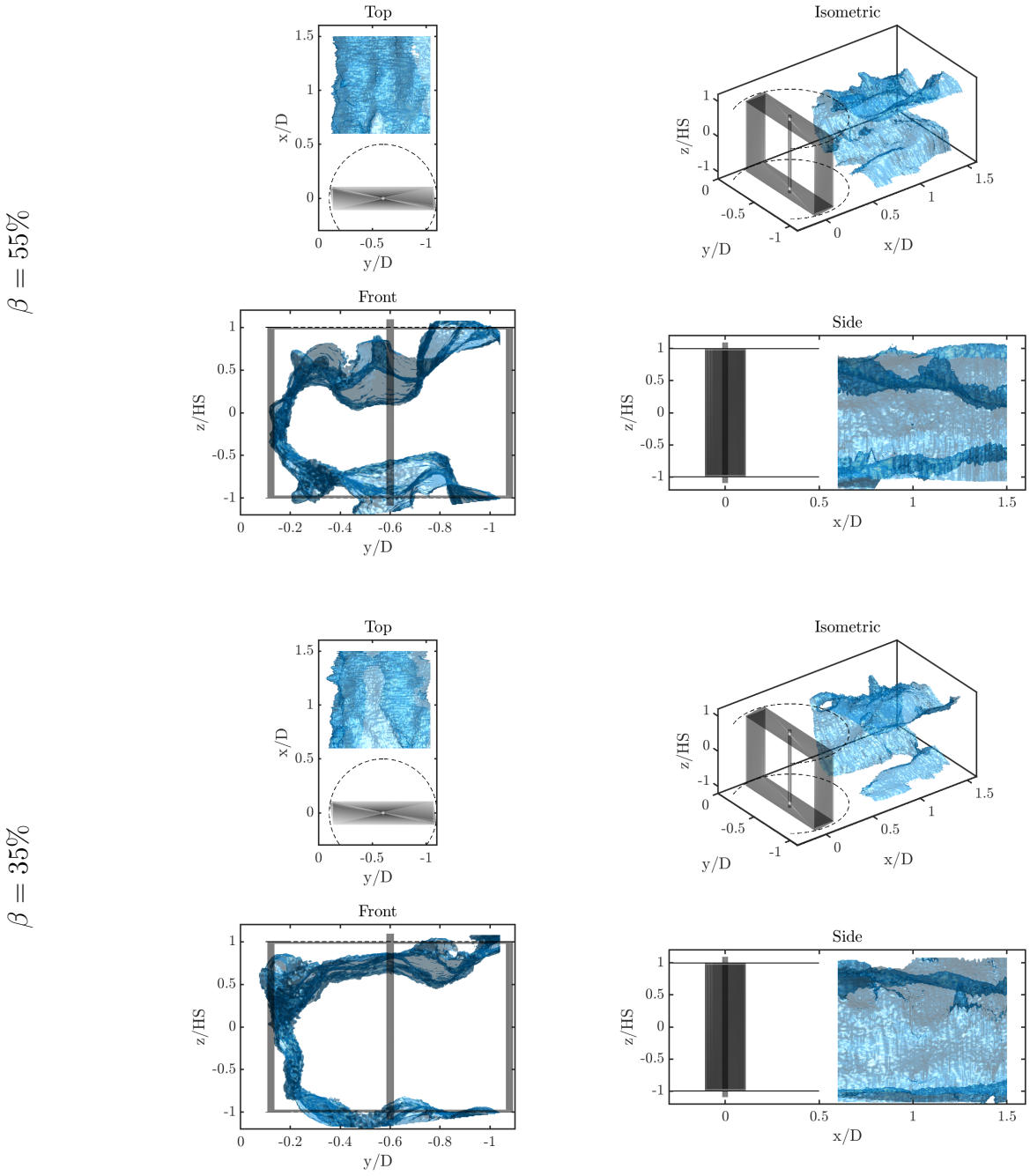

Figure 4.27: Wake structure and isosurface value set to $U_x = 75\%U_\infty$ $\theta = 0°$ $\beta = 35\%$ and 55%

lustrate the wake flow structure in Fig 4.27. For both blockages, the wake exhibits greater deformation at the top than at the bottom. From the top view, there is noticeable lateral skewing away from the center bypass due to the transition region expansion. The shear layer between the wake and the center bypass facilitates extensive mixing, leading to the transition region to expand laterally between the turbines and resulting in a reduction in the wake's cross-sectional area. This observation aligns with findings from [19], which noted that changes in wake size are more pronounced in the vertical (span-wise) direction than in the transverse direction.

Velocity component U_y is presented in Fig 4.28 for both cases. The cross-pattern vortices entrain only a small amount of fluid laterally into the center bypass, and this effect does not extend deeply into the wake region. The downwind tip vortex directs the top bypass fluid to the right, while the shear vortices, combined with the upwind tip vortex, push it to the left. Consequently, fluid is guided toward the center of the turbine and then is entrained into the wake by the downwash. In cases with $\beta = 35\%$, the tip vortices are weaker, and the top bypass appears to be predominantly influenced by vortices moving leftward.

Fig 4.29 showing the U_z velocity highlights that the mid-span lateral plane exhibits the lowest vertical velocity. The downstream tip vortices are primarily responsible for the strongest downward entrainment from the top bypass region. Additionally, significant downward entrainment is observed at the location coinciding with the upstream tip vortex. The figure also verifies that the high velocity present at the center mid-span is being convected away from the vertical center.

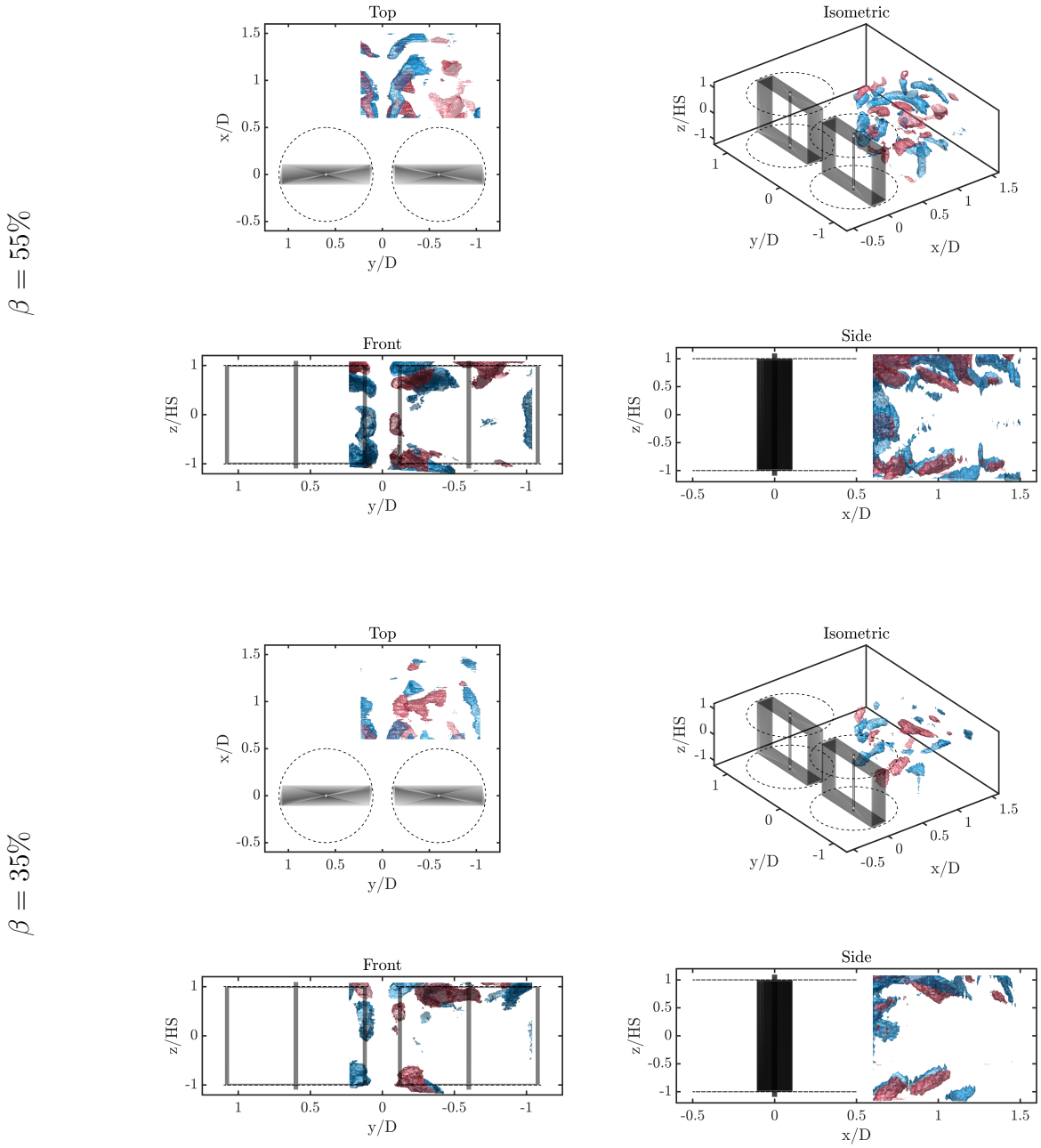

Figure 4.28: Blended volumetric isosurface for $U_y = \pm 30\% U_\infty$ $\theta = 0°$ $\beta = 35\%$ & 55%

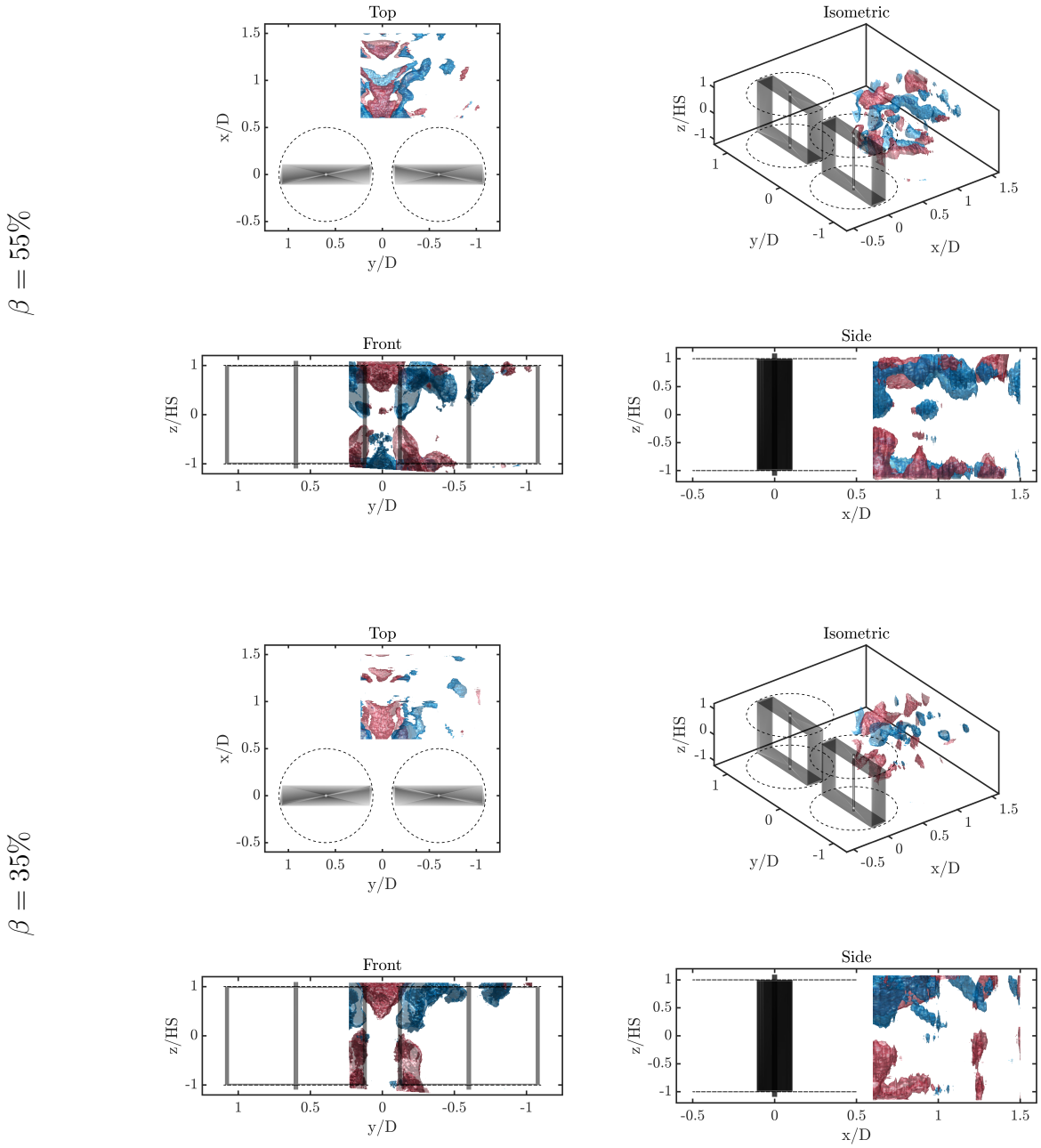

Figure 4.29: Blended volumetric isosurface for $U_z = \pm 30\% U_\infty$ $\theta = 0°$ $\beta = 35\%$ & 55%

Chapter 5

CONCLUSION

Stereo particle imagery velocimetry (PIV) data were collected from three downstream transverse planes (0.6D, 1.0D, and 1.5D) behind the center of a Cross Flow Turbine (CFT) array. Measurements were taken every three degrees of turbine phase angle (θ) from $0-180°$. This data were gathered at blockage levels $\beta = 35,\ 45,\ 55\%$ and at the tip speed ratio (λ) of optimal performance for each level of confinement. The goal was to study the three-dimensional fluid structure and its evolution in the near wake of the CFT array under high confinement.

The optimal λ was selected as 2.6, 2.9, and 3.6 for respective $\beta = 35,\ 45$, and 55%. The selections were based on measurements of the array's coefficient of power (C_p) as a function of λ for the given β levels. Test conditions are controlled to ensure that the Reynolds number (Re_D) and the Froude number (Fr_h) maintain constant across all β. A method was developed to calculate the convective velocity of streamwise vortex structures between successive planes of data, allowing the extrapolation of planar stereo PIV fields into a volumetric phase-dependent three-dimensional flow field for detailed analysis. The convective speed between successive streamwise locations was estimated and compared against the averaged flow's streamwise velocity (U) in different regions. All components of vorticity (ω) were estimated; however, there remains significant uncertainty regarding the non-x-components of vorticity. These components are particularly sensitive to errors in estimating convective velocity. Isosurfaces were utilized to indicate all components of vorticity and velocity within the volumetric reconstruction.

Time-averaged planar fields indicate that bypass velocity increases with β. The velocity deficit region becomes more contorted (not rectangular like the turbine projected area), while

the minimum velocity in the wake appears to not change significantly with confinement. The top and bottom symmetry planes descend downward as flow is convected downstream, indicating a downwash in the turbine wake. This downwash has a greater effect on the wake development at higher β, likely due to the lowered free surface. Phase-averaged analysis reveals that higher β levels create more complex and stronger vortices in the streamwise direction, impacting wake recovery. Notably, the wake size is smaller at $\beta = 55\%$ compared to the other cases. Both momentum and streamwise vorticity fields depend heavily on the turbine blade phase angle θ. The velocity profile exhibits some top and bottom symmetry, while the vorticity displays four-way antisymmetry about the centerline of the blades and the middle of the gap between the turbines. A high-velocity burst occurs every half rotation cycle when blades from both turbines align at $\theta = 180\ ^\circ$ and squeeze the flow between them. The vorticity field shows similar streamwise vortex profiles across all β levels. The major difference between the β values is that vorticity tends to be more concentrated in small regions with clearer boundaries at higher β, while it is more dispersed over a larger area at lower β levels. The strongest vortex structures are the tip vortices from the downstream blades, which appear to be attached to the blade. A cross pattern forms every half cycle, consisting of eight very distinct vortices for $\beta = 55\%$ & 45%. The number of vortices in this pattern decreases down to two for $\beta = 35\%$, likely due to entrainment from the less concentrated tip vortices. Downstream fields exhibit weaker vorticity and velocity, as a result of dissipation and momentum transfer.

The analysis of the estimated convective speed (U_c) indicates that it falls between the average speeds of the wake and the bypass. Specifically, U_c is closer to the higher bypass speed in the upstream interval from 0.6D to 1.0D, and it quickly decelerates to match the lower wake speed in the subsequent interval from 1.0D to 1.5D. Since the convective speed is calculated by tracking the vortices, and the most prominent vortices form near the boundary between the bypass and the wake region, this observed deceleration may result from the vortices mixing momentum between these two flow areas. The convective speed tends to decrease with β in both intervals.

In the volumetric reconstruction analysis, major streamwise vortex structures were classified into four categories: upstream and downstream blade tip vortices, cross-pattern vortices, and wake shear vortices. Hypotheses regarding the formation of each vortex type were proposed, supported by observational evidence. Specifically, the tip vortices appear to be generated by the pressure difference across the turbine blade, similar to that observed in three-dimensional wings. The downstream tip vortices are stronger than what is expected for the same blade operating in static flow due to the onset of dynamic stall and merging of high pressure of both blades as they approach close together at $\theta = 180°$. The cross-pattern vortices are observed in the center bypass at the turbine mid-span, created by strong tip vortex induction around $\theta = 0°$ and the four-way antisymmetry of the flow behind the turbine. This pattern is observed in all β but the antisymmetry becomes more distorted at lower β. The wake shear vortices are contributed by a streamwise vortex sheet generated by the wing strut and lateral shearing between the top and bottom bypass and the wake flow. The center shaft wake affects the wake shear vortices by bisecting the generated vortex sheet and consolidating the vortex filaments into larger vortex strips with greater strength. The hypothesized formations of the categorized vortex types require validation with data that can capture the near-blade dynamics of the same CFT array in high confinement.

The impact of each vortex type was examined using volumetric velocity isosurfaces: cross-pattern vortices were found to intensify local mixing, indicated by localized speed reduction, in the mid-span center bypass, downstream blade tip vortices facilitated the advection of high-speed flow from the center bypass to the top and bottom of the flow field, aiding in the entrainment of this flow into the wake. Meanwhile, top shear vortices, rotating in the same direction as the upstream blade tip vortices, primarily entrain flow from the top bypass into the wake, potentially leading to the collapse of the wake's upper and lower boundaries. Vortex structures for both high and low β cases work similarly, but since their strength increases with β level, these vortex structures can entrain faster bypass flow into the wake more quickly. As a result, the wake flow shrinks much faster in cross-sectional with higher blockage, suggesting a faster wake recovery. However, the stronger bypass also appears to

take longer to recover back to free stream velocity (U_∞).

The 3D reconstruction employed in this study generated relatively coherent fluid structures that transition smoothly across the investigated domain, spanning from 0.5 - 1.0D. The blending worked well to qualify the evolution of flow captured in each θ field. The calculated convective velocity produces coherent vortex structures and transits seamlessly between blended flow field estimates, suggesting the validity of Taylor's frozen flow hypothesis. However, it shows limitations in the flow section from 0.6D - 1.0D due to the faster convective speed and higher variation between the stronger vortices, especially for $\beta = 55\%$. Specifically, the lack of more than two data points to interpolate convective velocity causes an underestimation of convection in this forward section. This can be enhanced with more data planes to improve the estimation of convective velocity. The assumption that all vortex structures are convected at the same speed may also be less valid for this forward section.

Currently, there is a lack of high-resolution, three-dimensional, three-component, phase-dependent velocity measurements in turbine wakes. The flow visualizations generated in this study can provide valuable insights, potentially explaining performance correlations within blockage ratio β and tip speed. These insights could also help identify geometric parameters that could be adjusted to enhance the efficiency of CFT array designs at high confinement that promise large increases in power production.

REFERENCES

[1] Hunt, A. and Polagye, B., "Experimental techniques for evaluating the performance of high-blockage cross-flow turbine arrays," *Proceedings of the European Wave and Tidal Energy Conference*, Vol. 15, 2023.

[2] Ryan, K. J., Coletti, F., Elkins, C. J., Dabiri, J. O., and Eaton, J. K., "Three-dimensional flow field around and downstream of a subscale model rotating vertical axis wind turbine," *Experiments in Fluids*, Vol. 57, 2016.

[3] Hau, E., *Wind turbines: Fundamentals, technologies, application, economics*, Vol. 9783642271519, 2013.

[4] Brownstein, I. D., Wei, N. J., and Dabiri, J. O., "Aerodynamically interacting vertical-axis wind turbines: Performance enhancement and three-dimensional flow," *Energies*, Vol. 12, 2019.

[5] Dabiri, J. O., "Potential order-of-magnitude enhancement of wind farm power density via counter-rotating vertical-axis wind turbine arrays," *Journal of Renewable and Sustainable Energy*, Vol. 3, 2011.

[6] Schluntz, J. and Willden, R. H., "The effect of blockage on tidal turbine rotor design and performance," *Renewable Energy*, Vol. 81, 2015.

[7] Ferreira, C. S., Kuik, G. V., Bussel, G. V., and Scarano, F., "Visualization by PIV of dynamic stall on a vertical axis wind turbine," *Experiments in Fluids*, Vol. 46, 2009.

[8] Snortland, A., Polagye, B., and Williams, O., "Influence of Near-blade hydrodynamics on Cross-flow Turbine performance," *Proceedings of the 13th European Wave and Tidal Energy Conference*, 2019.

[9] Fujisawa, N. and Shibuya, S., "Observations of dynamic stall on turbine blades," *Journal of Wind Engineering and Industrial Aerodynamics*, Vol. 89, 2001.

[10] Castelli, M. R., Englaro, A., and Benini, E., "The Darrieus wind turbine: Proposal for a new performance prediction model based on CFD," *Energy*, Vol. 36, 2011.

[11] Howell, R., Qin, N., Edwards, J., and Durrani, N., "Wind tunnel and numerical study of a small vertical axis wind turbine," *Renewable Energy*, Vol. 35, 2010.

[12] Houlsby, G. T. and Vogel, C. R., "The power available to tidal turbines in an open channel flow," *Proceedings of Institution of Civil Engineers: Energy*, Vol. 170, 2017.

[13] Ari Athair, Owen Williams, B. P. A. H., "Performance and flow field characterization of a high-confinement cross-flow turbine array," .

[14] Gauvin-Tremblay, O. and Dumas, G., "Hydrokinetic turbine array analysis and optimization integrating blockage effects and turbine-wake interactions," *Renewable Energy*, Vol. 181, 2022.

[15] Consul, C. A., Willden, R. H., and McIntosh, S. C., "Blockage effects on the hydrodynamic performance of a marine cross-flow turbine," *Philosophical Transactions of the Royal Society A: Mathematical, Physical and Engineering Sciences*, Vol. 371, 2013.

[16] Miller, M. A., Duvvuri, S., Brownstein, I., Lee, M., Dabiri, J. O., and Hultmark, M., "Vertical-axis wind turbine experiments at full dynamic similarity," *Journal of Fluid Mechanics*, Vol. 844, 2018.

[17] Westerweel, J. and Scarano, F., "Universal outlier detection for PIV data," *Experiments in Fluids*, Vol. 39, 2005.

[18] Kendall, M. G., "Rank Correlation Methods." *Biometrika*, Vol. 44, 1957.

[19] Ross, H. and Polagye, B., "An experimental evaluation of blockage effects on the wake of a cross-flow current turbine," *Journal of Ocean Engineering and Marine Energy*, Vol. 6, 2020.

[20] Ross, H. and Polagye, B., "An experimental assessment of analytical blockage corrections for turbines," *Renewable Energy*, Vol. 152, 2020.

[21] Bachant, P. and Wosnik, M., "Characterising the near-wake of a cross-flow turbine," *Journal of Turbulence*, Vol. 16, 2015.

[22] Strom, B., Polagye, B., and Brunton, S. L., "Near-wake dynamics of a vertical-axis turbine," *Journal of Fluid Mechanics*, Vol. 935, 2022.

[23] Tescione, G., Ragni, D., He, C., Ferreira, C. J. S., and van Bussel, G. J., "Near wake flow analysis of a vertical axis wind turbine by stereoscopic particle image velocimetry," *Renewable Energy*, Vol. 70, 2014.

[24] Riccardo Zamponi, S. M. and Schram, C., "Rapid distortion theory of turbulent flow around a porous cylinder," *Journal of Fluid Mechanics*, Vol. 12, 2017.